Müller *et al. Clinical Epigenetics* (2026) 18:76
https://doi.org/10.1186/s13148-026-02133-w

Clinical Epigenetics

RESEARCH Open Access

GLYATL1 is associated with metabolic and epigenetic changes and with endocrine resistance in luminal breast cancer

Janina Müller[1,2†], Emre Sofyali[1,2†], Luisa Schwarzmüller[1,2†], Yael Aylon[3], Eviatar Weizman[4], Lisa Schlicker[5], Katherine Kelly[2,6], Simone Borgoni[1,2], Simin Oz[6], Cole Stocker[1,2], Sara Burmester[1], Angelika Wörner[1], Sabine Karolus[1], Birgitta E. Michels[1], Daniela Heiss[7], Rainer Will[7], Veronica Rodrigues de Melo Costa[1], Pavlo Lutsik[6], Dieter Weichenhan[6], Ilse Hofmann[8], Nishanth Belugali Nataraj[9,10], Yosef Yarden[9], Luca Magnani[11,12], Christoph Plass[6], Almut Schulze[5], Cindy Körner[1], Moshe Oren[3] and Stefan Wiemann[1*]

Abstract

Background Estrogen receptor alpha (ERα)-positive luminal breast cancer is commonly treated with aromatase inhibitors (AI) to block estrogen signaling; however, resistance frequently develops, limiting therapy success.

Results We observed that *GLYATL1* (Glycine-N-Acyltransferase Like 1) expression is upregulated in AI-resistant breast cancer cell models and in patients undergoing AI therapy, correlating with poorer survival. Here we demonstrate that GLYATL1 promotes resistance to estrogen deprivation by elevating succinate levels and altering epigenetic histone marks associated with active transcription. Knockdown or knockout of *GLYATL1* reverses these effects and reduces proliferation under estrogen-deprived conditions. Notably, *GLYATL1* expression is positively regulated by estrogen receptor alpha signaling, however, independently of estrogen.

Conclusions These findings reveal GLYATL1 as a metabolic and epigenetic mediator of endocrine therapy resistance, suggesting it as a potential target to overcome AI resistance in luminal breast cancer.

Keywords Luminal breast cancer, Estrogen-receptor alpha (ERα), Aromatase inhibition, Endocrine therapy resistance, GLYATL1

†Janina Müller, Emre Sofyali and Luisa Schwarzmüller have contributed equally to this work.

*Correspondence:
Stefan Wiemann
s.wiemann@dkfz.de

Full list of author information is available at the end of the article

Background

Breast cancer remains the most prevalent malignancy and the second leading cause of cancer-related mortality among women globally [1, 2]. It is a heterogeneous disease, requiring molecular subtyping in clinical practice. This classification is based on the expression of estrogen receptor alpha (ERα), progesterone receptor (PR), human epidermal growth factor receptor 2 (HER2), and the proliferation marker protein Ki-67 [3]. Approximately two-thirds of breast tumors are classified as ER-positive (ER+), mostly corresponding to luminal subtypes [4]. Patients with such luminal-like disease typically receive endocrine therapies designed to interfere with estrogen signaling. These therapy approaches either target ERα directly, or prevent estrogen synthesis by inhibiting the essential enzyme aromatase (CYP19A1) with aromatase inhibitors (AI), thereby depriving the cancer cells, and the patient, of estrogen [5]. Despite the initial efficacy of endocrine therapies, up to 40% of patients presenting with locally advanced disease at the time of diagnosis relapse during or after endocrine therapy [6]. However, resistance acquisition is a highly individual process that may involve various mechanisms, including the activation of alternative signaling pathways [7, 8], acquisition of mutations in *ESR1,* the gene encoding ERα [9, 10], metabolic rewiring [11], and epigenetic reprogramming [12, 13]. These mechanisms contribute to inter- and intratumor heterogeneity and allow tumors to sustain growth independently of estrogen [14, 15]. Uncovering further resistance mechanisms is of key relevance to facilitate the development of personalized therapeutic approaches.

Along these lines, we characterized long-term estrogen deprived (LTED) sublines of two ER + breast cancer cell line models (MCF7 and T47D), modeling resistance to aromatase inhibition. Multi-omics profiling of cells resistant to estrogen-deprivation included RNA sequencing, ATAC-sequencing, methylation array analysis, metabolomics, and proteomic profiling. We identified significant alterations in gene expression and chromatin accessibility as well alterations at metabolite, proteomic, and epigenomic levels. Among the top deregulated genes was Glycine-N-Acyltransferase Like 1 (*GLYATL1*), which was upregulated in both in vitro models, and whose expression is associated with poorer overall survival in Luminal A breast cancer patients. GLYATL1 is Glycine-N-Acyltransferase Like 1/glutamine-*N*-acyltransferase and catalyzes the transfer of an acyl group to the N-terminus of glutamine [16]. While GLYATL1 has been implicated in tumor growth and disease progression across various cancer types including breast cancer (17—19), its potential role in endocrine resistance in luminal breast cancer remains poorly understood.

Here, we present a comprehensive investigation of GLYATL1, delineating its functional role in sustaining a resistance phenotype, and its critical impact on cell proliferation, on mediating succinate accumulation and on epigenetic reprogramming under estrogen-deprived conditions. We further explore the regulatory mechanisms underlying *GLYATL1* expression, suggesting that this is regulated by estrogen-independent ERα activity specifically in LTED cells. These findings highlight GLYATL1 as a potential biomarker and therapeutic target for addressing endocrine resistance to aromatase-inhibition in ER + breast cancer.

Methods

Cell lines

MCF7 (RRID:CVCL_0031) was obtained from ATCC (Manassas, VA, USA). T47D (RRID:CVCL_0553) and HEK293FT (RRID:CVCL_6911) were obtained from LGC Standard GmbH (Wesel, Germany). These parental cell lines were cultivated in Dulbecco's Modified Eagle Medium (DMEM #11,574,486, Gibco, Thermo Fisher Scientific, Waltham, MA, USA) supplemented with 10% FBS (#26,140,079, Gibco, Thermo Fisher Scientific, Waltham, MA, USA), 10 nM 17-β-estradiol (E8875, Sigma-Aldrich, Saint-Louis, MI, USA), 2 mM L-glutamine (#25,030,081, Gibco, Thermo Fisher Scientific, Waltham, MA, USA), 1 mM sodium pyruvate (#11,360,070, Gibco, Thermo Fisher Scientific, Waltham, MA, USA), and 50 units/mL penicillin / 50 µg/mL streptomycin sulfate (#15,140,122, Gibco, Thermo Fisher Scientific, Waltham, MA, USA), and incubated at 37 °C with 5% CO_2 in a humidified incubator. Long-term estrogen-deprived (LTED) MCF7 and T47D cells were cultured in DMEM (w/o phenol red, #31,053,028) supplemented with 10% charcoal-stripped FBS (#12,676,029), 2 mM L-glutamine (#25,030,081), 1 mM sodium pyruvate (#11,360,070), and 50 units/mL penicillin / 50 µg/mL 50 µg/mL streptomycin sulfate (#15,140,122, all Gibco, Thermo Fisher Scientific, Waltham, MA, USA), until the cells proliferated similar to parental MCF7 and T47D cells, respectively [20, 21]. All cell lines were regularly authenticated by STR profiling (Multiplexion GmbH Heidelberg, Germany) and were tested free of mycoplasma contamination.

Generation of stable GLYATL1 knockout clones with CRISPR/Cas9

GLYATL1 was knocked out in the MCF7 LTED cell line using CRISPR/Cas9 technology by co-transfection of cells with a sgRNA (guide-sequence: 5′-GUUU CUUCUUCAAGGUCUCA-3′) (Synthego, Redwood City, CA, USA) targeting exon 3 (Reference transcript: NM_001389711.2) of the *GLYATL1* gene, and SpCas9 Nuclease protein (#R20SPCAS9-Sm, Synthego, Redwood City, CA, USA). Co-transfection was performed using Lipofectamine CRISPRMAX Cas9 transfection reagent (#CMAX00001, Thermo Fisher Scientific, Waltham,

MA, USA) according to the manufacturer's instructions. Knockout cultures were cultivated in the same media and conditions as the LTED cells. Single clones were isolated in 96-well plates utilizing an F.SIGHT single-cell dispenser (Cytena, Freiburg, Germany). PCR primers were designed upstream of exon 3 (forward primer: 5′-AAAA TCTATGCCTACTCCTGCTCC-3′) and downstream of exon 4 (reverse primer: 5′-TGCTTTACACGAAGGGTG GG-3′) within the *GLYATL1* gene to amplify the region of the CRISPR knockout (expected size of PCR product in the genome w/out KO: 1543 bp), using Phusion Hot Start II DNA-Polymerase (2 U/µL) (#F549L, Thermo Fisher Scientific, Waltham, MA, USA). The thermocycling protocol included: 98 °C–2 min, 35× (98 °C–10 s, 64 °C–20 s, 72 °C–60 s), and 72 °C–10 min final extension. PCR products were analyzed by agarose gel electrophoresis and bands were gel-purified using the Wizard SV Gel and PCR Clean-up System (#A9281, Promega, Madison, WI, USA), according to the manufacturer's instructions. Sanger-sequencing was performed (Eurofins Genomics Germany GmbH, Ebersberg, Germany) using the forward and reverse PCR-primers. and sequences analyzed using SnapGene software (Dotmatics, Bishop's Stortford, UK). Two clones (KO1 and KO2) were selected based on a predicted knockout by SnapGene. Both clones had shown two bands of about 1100 and 1500 bp in the agarose gel. Sequences of the DNA in the respective bands were mapped to hg38 using the BLAT-tool in the UCSC genome browser [22] to assess the impact of deletions on the gene structure.

RNA-sequencing

RNA was extracted using the RNeasy Mini kit (#74,104, Qiagen, Hilden, Germany) according to the manufacturer's instructions and RNA-sequencing was performed at the DKFZ NGS Core Facility, using different protocols for MCF7 parental and LTED, vs. MCF7 LTED and *GLYATL1* knockout clones KO1 and KO2. MCF7 parental and LTED conditions: RNA-seq libraries were prepared using the Illumina TruSeq RNA Library Preparation Kit (Illumina, San Diego, CA, USA) and sequenced on an Illumina HiSeq 4000 platform (Illumina, San Diego, CA, USA), generating on average 45 million paired-end reads with a length of 2 × 100 base pairs. Sequencing reads were pre-processed using a combination of open-source tools and *in-house* scripts. Quality filtering and artifact removal were carried out using the FastX Toolkit v0.0.13 (https://github.com/agordon/fastx_toolkit), specifically employing *fastq_quality_filter* with parameters -q 20 -p 90 and *fastx_artifacts_filter*. Poly-A tails were trimmed using HOMER tools v4.7 [23] with the trim -3 AAAAAAAAA command. Reads containing ambiguous bases ('N') or characters outside the canonical nucleotide set (A, C, G, T, U) were removed using custom in-house Perl scripts. Additionally, reads shorter than 17 bases or longer than 10,000 bases were excluded. To ensure proper pairing after these filtering steps, orphaned reads were discarded using an in-house script. Ribosomal RNA (rRNA) contamination was removed if the alignment rate against rRNA sequences exceeded 1%. For this purpose, reads were first aligned to an rRNA reference using Bowtie2 v2.2.4 [24]. Where necessary, rRNA-aligned reads were filtered out using samtools *view* v0.1.18 [25] with flags -f 12 -F 256, and the remaining reads were converted back to FASTQ format using *SamToFastq* from Picard tools v1.78 (https://broadinstitute.github.io/picard/). Duplicate reads were removed using Sambamba v0.6.5 [26] with the *sort* and *markdup* commands executed consecutively. Reads were aligned to the human reference genome GRCh38.p13 using STAR aligner v2.3 [27], and gene-level quantification was performed using HTSeq-count v0.6.0 [28]. GENCODE release 34 was used for annotation during both alignment and read counting. Differential gene expression analysis was performed with DESeq2 v1.28.1 [29] with differentially expressed genes identified at a false discovery rate (FDR) threshold of 0.05.

MCF7 LTED and LTED *GLYATL1* knockout KO1 and KO2: RNA libraries were prepared using the TruSeq Stranded RNA Library Prep Kit (Illumina, San Diego, CA, USA) according to the manufacturer's protocol. Sequencing was conducted on the Illumina NovaSeq 6000 platform (Illumina, San Diego, CA, USA), generating paired-end reads with a length of 2 × 100 base pairs (S1 flow cell). Each sample yielded an average of approximately 59 million read pairs. Quality control of the raw sequencing data was performed using FastQC v0.11.9 (https://www.bioinformatics.babraham.ac.uk/projects/fastqc/). Strand-specific reads were aligned to the human reference genome GRCh38.p13 using STAR v2.5.2a [27], with the genome index generated from GENCODE v34 annotations. Genome-wide similarity between sequencing replicates was evaluated using deepTools v3.5.2 [30]. Gene-level read counts were obtained using the htseq-count tool from HTSeq v0.11.1 [28]. Differential gene expression analysis was performed with DESeq2 v1.40.2 [29], comparing the indicated cell lines. Genes with fewer than 10 total reads across all samples were excluded from the analysis. Differentially expressed genes were identified at an FDR threshold of 0.05.

ATAC-sequencing

Libraries for ATAC-sequencing were prepared with modifications based on published protocols [31]. Cells were lysed using 1% NP40, followed by tagmentation at 55 °C for 8 min in a reaction mixture consisting of 2.5 µL of TDE1 (Nextera Illumina DNA Kit, Illumina, San Diego, CA, USA), 25 µL of tagmentation buffer (Nextera

Illumina DNA Kit), and 25 µL of the lysed cells. The tagmentation reaction was terminated by the addition of 10 µL of 5 M guanidine thiocyanate, and samples were subsequently purified with AMpure Beads (Beckman Coulter, Brea, CA, USA). Library construction was performed using NEBNext High Fidelity PCR Mix, and sequencing (> 5 million reads/sample) was conducted on an Illumina HiSeq 2500 platform at the DKFZ NGS Core Facility. Sequencing reads were processed to remove adapter sequences using TrimGalore (v.0.6.7). Trimmed reads were aligned to the hg38 canonical reference using Bowtie2 (v.2.4.2) with very sensitive end-to-end presets [24]. A maximum fragment length of 1000 was selected for paired alignments and mate dovetailing was allowed. Alignments were filtered to remove mitochondrial reads, non-proper pairs and reads with mapping quality score < 30. Duplicates were removed using Picard MarkDuplicates (v.2.18.2.2, http://broadinstitute.github.io/picard). Peak calling was performed using MACS2 (v.2.2.9.1) [32] using the parameters "–qvalue '0.05' –nomodel –extsize '200' –shift '-100'". All identified peaks were merged to create a common bed file containing read counts, which was then utilized for differential analysis using edgeR (v3.36.0) [33]. Heatmaps of differential accessibility were created using ChIPpeakAnno (v3.0.0) [24, 34] and ComplexHeatmap (v2.8.0) summarizing log2 fold changes across 40 bins around the TSS of each gene.

EPIC 850 k methylome array

Total DNA was extracted from MCF7 parental and LTED cells using the DNeasy Blood and Tissue Kit (Qiagen, Hilden, Germany), following the manufacturer's protocol. Methylation profiling was performed by the DKFZ Microarray Core Facility using the Illumina MethylationEPIC BeadChip platform (Illumina, San Diego, CA, USA). Quality control, filtering and normalization were performed using Rnbeads (v.2.21.3) [35]. Probes overlapping with single nucleotide polymorphisms (SNPs), cross-reactive probes, those outside of CpG context and those mapping to sex chromosomes were filtered out. Probes with detection p-value > 0.05 and sites covered by fewer than three beads were further excluded. Normalization and background subtraction were carried out using the "scaling.internal" and "sesame.noobsb" methods of Rnbeads. Methylation beta-values were summarised by mean across each pair of replicates and the difference in mean methylation was calculated per-CpG as a measure of differential methylation between parental and LTED cells.

Immunofluorescence imaging

For recombinant expression of the GLYATL1 protein, the *GLYATL1* open reading frame was cloned from a Gateway entry clone (pENTR223-GLYATL1, IMAGE:100,071,537) [36] into a Gateway-compatible expression vector (pFLAG-C) to obtain plasmid pFLAG-C-GLYATL1, which encodes a protein with a FLAG-tag fused to the C-terminus of GLYATL1. MCF7, T47D and HEK293 cells were transiently transfected with pFLAG-C-GLYATL1 plasmid and grown on 12 mm coverslips until reaching 70–80% confluency. Mitochondria were stained with 500 nM abberior LIVE ORANGE mito (LVORANGE, Abberior, Göttingen, Germany) for 1 h at 37 °C in 5% CO_2. Subsequently, cells were fixed with 4% formaldehyde for 15 min at room temperature and permeabilized with 0.1% Triton X-100 in PBS for 10 min. To prevent non-specific binding, cells were incubated with 3% BSA in PBS for 1 h at room temperature. Mouse anti FLAG antibodies (1:1000, #F3165, Sigma Aldrich, St. Louis, MI, USA) in 3% BSA were then added and incubated overnight. Following three washing steps with PBS, secondary goat anti mouse antibodies conjugated to alexa-488 (1:400, #ab150113, Abcam, Cambridge, UK) were added and incubated for 1 h at room temperature in the dark. After washing off excess secondary antibodies with PBS, cells were mounted onto glass slides using ProLong Diamond antifade mounting media with DAPI (#P36966, Thermo Fisher Scientific, Waltham, MA, USA). Samples were examined using a fluorescence microscope (LSM-900, Zeiss, Oberkochen, Germany). Negative controls, which lacked primary or secondary antibodies, were included to verify specificity and antibody reactivity. Analysis of images was performed using Zen Blue software (Carl Zeiss, Jena, Germany) and ImageJ (https://imagej.net/ij/). Manders' coefficient [37] was calculated using the JACoP in ImageJ to quantify the degree of colocalization between fluorophores.

Western blot

Cell were lysed using RIPA buffer (#89,900, Thermo Fisher Scientific, Waltham, MA, USA) supplemented with cOmplete EDTA-free protease inhibitor (#11,697,498,001; Merck, Darmstadt, Germany) and PhosSTOP phosphatase inhibitor (#4,906,845,001; Merck, Darmstadt, Germany). Following incubation on ice for 30 min, lysates were centrifuged for 30 min at 15,000 xg and 4 °C. Protein concentration of the supernatant was measured utilizing Pierce™ BCA Protein Assay Kit (#23,250, Thermo Fisher Scientific, Waltham, MA, USA). Proteins from cell lysates and PageRuler™ Prestained Protein Ladder (#26,616, Thermo Fisher, Waltham, MA, USA) as size maker were separated by SDS-PAGE [38]. Proteins were blotted using Trans-Blot Turbo™ Mini PVDF Transfer Packs and the Trans-Blot Turbo™ Transfer System (Bio-Rad Laboratories, Hercules, CA, US) according to the manufacturer's instructions. Membranes were blocked in Blocking Buffer for Fluorescent Western Blotting (MB-070, Rockland, Philadelphia,

PA, USA): TBS supplemented with 10 mM NaF and 1 mM Na_3VO_4. Subsequently, the membranes were incubated with a rabbit anti GLYATL1 antibody (1:1,000 dilution, #PA039501, Sigma-Aldrich, Taufkirchen, Germany) in blocking buffer at 4 °C overnight. The next day, membranes were washed three times for 5 min each with TBS containing 0.1% Tween 20 (TBST #91,414, Merck, Taufkirchen, Germany). Then, blots were incubated with a goat anti-rabbit (Alexa Fluor™ 680 conjugated, 1:10,000 dilution, #A-21077, Thermo Fisher Scientific, Waltham, MA, USA) secondary antibody, and washed again. Proteins were visualized with a LI-COR Odyssey 9120 scanner (LI-COR, Lincoln, NE, USA) scanning in the 700 and 800 nm channels for Alexa Fluor™ 680 and DyLight™ 800 fluorophores, respectively. Then, gels were incubated with a mouse anti ß-Actin (1:10,000 dilution, #0869100-CF, MP Biologicals, Irvine, CA, USA, 1:1500 dilution) over night, and washed three times for 5 min each with TBS containing 0.1% Tween 20. A goat anti-mouse (DyLight™ 800 4X PEG conjugated, 1:10,000 dilution, #SA5—35,521, Thermo Fisher Scientific, Waltham, MA, USA) was used to visualize actin bands with a LI-COR Odyssey 9120 scanner (LI-COR, Lincoln, NE, USA) scanning in both, 700 and 800 nm channels for Alexa Fluor™ 680 and DyLight™ 800 fluorophores, respectively.

Single-pot solid-phase sample preparation (SP3) for proteome measurements

Single-pot solid-phase sample preparation (SP3) was performed using 20 µg of protein in a total volume of 60 µL of RIPA buffer (#89,900, Thermo Fisher Scientific, Waltham, MA, USA), supplemented with 100 mM triethylammonium bicarbonate (TEAB). To facilitate protein reduction and alkylation, chloracetamide (CAA) and tris(2-carboxyethyl)phosphine (TCEP) were added to final concentrations of 40 mM and 10 mM, respectively, and the mixture was incubated at 95 °C for 5 min. Subsequently, 1 µL of each type of paramagnetic bead (#45,152,105,050,250 and #65,152,105,050,250; Sigma-Aldrich, St. Louis, MO, USA) was mixed in a 1:1 ratio. Ethanol was added to achieve a final concentration of 50%, and the mixture was incubated for 15 min at 650 rpm. To enhance bead-protein binding, the sample was shaken at room temperature for an additional 15 min at the same speed. Bound proteins were washed twice with 80% ethanol, followed by a single wash with 100% acetonitrile. After aspirating any residual acetonitrile, the beads were resuspended in 100 mM TEAB containing trypsin at a protease-to-protein ratio of 1:25. Digestion was facilitated by sonication in a water bath for 30 s, followed by incubation at 37 °C while shaking at 800 rpm for 16 h. The next day, the supernatant containing the digested peptides was collected and vacuum-dried in a speed-vac at 30 °C and 1300 rpm. The resulting peptides were stored at -20 °C until further analysis.

Liquid chromatography (LC) separation of peptides

Peptides were solubilized in mass spectrometry (MS)-grade water supplemented with 0.1% trifluoroacetic acid (TFA) and 2.5% hexafluoroisopropanol (HFIP) prior to analysis. Using an UltiMate 3000 liquid chromatography (LC) system (Thermo Fisher Scientific, Waltham, MA, USA) 1 µg of peptides were separated on a 25 cm column (#186,008,795, Waters nanoEase™ BEH C18, 130 Å, 1.7 µm, 75 µm × 250 mm, Waters, Milford, MA, USA). A linear gradient of acetonitrile from 4 to 30% over 100 min at a flow rate of 300 nL/minute was employed, culminating in a total method duration of 120 min for peptide separation.

Parallel reaction monitoring (PRM) mass spectrometry (MS) measurements

Mass spectrometric analysis was performed using an Orbitrap Exploris 480 (Thermo Fisher Scientific, Waltham, MA, USA), with MS1 scans acquired at a resolution of 120,000 and an automatic gain control (AGC) target set to 3e6 ions. This approach ensured high sensitivity and resolution during the analysis of the peptide samples. The MS2 spectra were collected for pre-selected peptides of GLYATL1 at a resolution of 120,000. Data analysis was conducted using Skyline (version 3.1.0.7312). The GLYATL1 protein FASTA files were sourced from UniProt (Q969I3) and subjected to in silico digestion with trypsin, permitting one missed cleavage site. The identification of Y and b fragment ions facilitated the selection of filtered peptides corresponding to three pre-measured GLYATL1 peptides. The retention time of the peptide R.ALLLVTEDILK.L was determined using spectra from an MCF7 cell line stably overexpressing *GLYATL1*. This retention time was subsequently applied across all samples. Peak areas were computed by defining peak boundaries and summing the areas of the fragment ions.

Data-independent acquisition (DIA) for total proteome analysis

MS1 spectra were acquired using an Orbitrap Exploris 480 (Thermo Fisher Scientific, Waltham, MA, USA) at a resolution of 120,000 and a maximum of 3e6 ions were collected for each spectrum. MS2 spectra were acquired in 47 isolation windows of variable width covering 400–1000 m/z. The peptides were fragmented with a collision energy of 28%, the MS2 resolution was 60,000 and up to 1e6 ions were collected for each spectrum. Using Spectronaut (version 15.6; Biognosys, Schlieren, Switzerland) proteins were identified by searching the raw data against the proteome-wide human fasta file (79,052

entries, downloaded from Uniprot 15.03.2022). Up to two missed cleavage sites by trypsin were allowed, carbamidomethylation (C) was set as a fixed modification, oxidation (M) and acetylation (N-terminus) as variable modifications. Peptides were quantified on the MS2 level by summing up the signal area under the curve of the 3–6 highest abundant fragment ions. Proteome data were further analyzed using R (version 4.3.1). Protein intensities were log2 transformed and principal component analysis was performed using the prcomp() function. For statistical analysis, *p*-values were computed using unpaired, two-sided t-tests for proteins that were identified and quantified in all six samples of a given comparison. Benjamini–Hochberg adjustment [39] was applied to correct *p*-values for multiple hypothesis testing.

Metabolite extraction

For extraction of polar metabolites, cells ($\sim 1 \times 10^6$) were washed with cold ammonium acetate (154 mM) and scraped off in 0.5 mL ice-cold MeOH/H_2O/Acetonitrile (50/20/30 v/v) containing internal standards (stable isotope labeled amino acids and $^{13}C_3$-Malonyl-CoA as well as deuterium labeled TCA cycle intermediates, Cambridge Isotope laboratories, Tewsbury, MA, USA). After vortexing and sonication, samples were centrifuged at 13,000 × g for 5 min and the supernatant was applied onto a C18 8B-S001-DAK solid phase column (Phenomenex, Torrance, CA, USA), previously activated using acetonitrile and equilibrated using MeOH/H_2O/Acetonitrile (50/20/30 v/v). The remaining pellet was extracted one more time using 0.5 mL ice-cold MeOH/H_2O/Acetonitrile (50/20/30 v/v). The eluate was dried in a refrigerated vacuum concentrator (Labconco, Kansas City, MO, USA) at 10 °C overnight. The residual pellet was used for protein quantification by BCA assay according to the instructions from the manufacturer. For this, the pellet was dissolved in 0.2 M NaOH and incubated for 20 min at 95 °C.

LC–MS measurement of metabolites

LC–MS measurement of metabolites was performed on an Ultimate 3000 coupled to a Q Exactive Plus mass spectrometer (Thermo Fisher Scientific, Waltham, MA, USA). Dried metabolite extracts were dissolved in 100 µL 5 mM NH_4OAc in CH_3CN/H_2O (75/25, v/v), and 3 µL were applied onto an amide-HILIC column (16,726–012105, 2.6 µm, 2.1 × 100 mm, Thermo Fisher Scientific, Waltham, MA, USA), where the temperature was kept at 30 °C. The following solvents were used: solvent A consisting of 5 mM NH_4OAc in CH_3CN/H_2O (5:95, v/v) and solvent B consisting of 5 mM NH_4OAc in CH_3CN/H_2O (95:5, v/v). The following gradient was applied: 98% solvent B for 2 min, followed by a linear decrease to 40% solvent B within 5 min, then maintaining 40% solvent B for 13 min, then returning to 98% solvent B within 1 min and maintaining 98% solvent B for 5 min for column equilibration before each injection. The flow rate was maintained at 350 µL/minutes. The eluent was directed to the HESI source from 1.5 min to 21.0 min after sample injection and the following HESI source parameters were applied: Sheath gas flow rate—30, Auxiliary gas flow rate—10, Spray voltage—3.6 kV (pos)/ 2.5 kV (neg), Capillary temperature—320 °C, S-lens RF level—55.0. For the detection of acyl-CoAs, acquisition was done in positive mode with a scan range from 760 to 1100 m/z, a resolution of 70,000, AGC target of $1E^6$, and maximum injection time of 50 ms. For data-dependent MS2 (ddMS2), the resolution was set to 17,500, AGC target to $5E^4$, maximum injection time of 50 ms and stepped collision energies of 20, 50 and 80. For broad-spectrum detection of water-soluble metabolites, the acquisition was performed in polarity switching mode within the scan range of 69–1000 m/z, with otherwise similar settings and ddMS2. Peaks corresponding to the calculated metabolite masses taken from an in-house metabolite library were integrated using the El-MAVEN software (https://docs.polly.elucidata.io/Apps/Metabolomic Data/El-MAVEN.html) and metabolite identification was supported by fragmentation patterns [40]. Peak intensities were normalized by their respective internal standard levels.

Epigenetic-focused cytometry time-of-flight (EpiTOF)

MCF7 (parental, LTED, LTED *GLYATL1* KO1 and KO2) single-cell suspensions were generated and washed with Maxpar PBS (#201,058, Fluidigm, San Francisco, CA. USA) and subsequently stained with 1.25 µM Cisplatin for one minute to identify dead cells. The staining reaction was quenched using DMEM supplemented with 10% FBS. Cells were washed with Maxpar Cell Staining Buffer (#201,068, Fluidigm, San Francisco, CA, USA), and about 3×10^6 cells per sample were fixed, permeabilized using the Maxpar Nuclear Antigen Staining Buffer Set (#201,063, Fluidigm, San Francisco, CA, USA), and barcoded with the Cell-ID 20-Plex Pd Barcoding Kit (#201,060, Fluidigm, San Francisco, CA, USA) according to the manufacturer's instructions. Following two washing steps with Maxpar Nuclear Antigen Staining Buffer Set permeabilization buffer, equal amounts of barcoded samples of the different MCF7 cell lines (i.e., parental, LTED, LTED *GLYATL1* KO1 and KO2) were combined and incubated with an antibody cocktail (Supplementary Table 11) for 30 min at room temperature. Following antibody incubation, the cells were washed twice with Maxpar Cell Staining Buffer and fixed at 4 °C with fresh 4% formaldehyde (#28,908, Thermo Fisher Scientific, Waltham, MA, USA), ensuring gentle rocking to prevent clumping. Following overnight incubation, 125 nM Cell-ID Intercalator-Ir (#201192A, Fluidigm, San Francisco,

CA, USA) was added and incubated for 45 min at room temperature to label DNA. Afterward, cells were washed twice with Maxpar Cell Staining Buffer and once with Maxpar Water (#201,069, Fluidigm, San Francisco, CA, USA). Cells were resuspended in a dilution of EQ Four Element Calibration Beads (#28,908, Fluidigm, San Francisco, CA, USA) in Maxpar Water, achieving a concentration of approximately 250 K cells/ml, and subsequently filtered through a 35 µm mesh. Data was acquired on a CyTOF Helios platform (Fluidigm, San Francisco, CA, USA). Normalization and data cleanup to isolate live single cells were conducted as described by Bagwell et al. [41]. Metal-conjugated antibodies (Supplementary Table 11) were either obtained from Fluidigm or conjugated utilizing appropriate Maxpar X8 Antibody Labeling Kits (Fluidigm, San Francisco, CA, USA). The mass cytometry antibody panel was designed to minimize signal spillover utilizing the Maxpar Panel Designer (Fluidigm, San Francisco, CA, USA). Analysis of EpiTOF data was executed through an R-based pipeline [42]. Data were imported into R (version 4.0.2) and transformed using arcsine transformation with a cofactor of 5 and regressed to H3 and H3.3 expression. For statistical comparison, the median arcsine-transformed intensities were used (n = 2). Using a two-sided, unpaired T-test, LTED was compared against the parental cells and cells from both GLYATL1 KO clones simultaneously.

Cell proliferation assay

Cells were plated into black clear F-bottom 96-well plates (#655,090, Greiner Bio-One International GmbH, Kremsmünster, Austria) and cultivated for seven days. Parental cells were cultivated in DMEM (#11,574,486, Gibco, Thermo Fisher Scientific, Waltham, MA, USA) supplemented with 10% FBS (#26,140,079, Gibco, Thermo Fisher Scientific, Waltham, MA, USA), 10 nM 17-β-estradiol (E8875, Sigma-Aldrich, Saint-Louis, MI, USA), 1 mM sodium pyruvate (#11,360,070, Gibco, Thermo Fisher Scientific, Waltham, MA, USA), 2 mM L-glutamine (#25,030,081, all Gibco, Thermo Fisher Scientific, Waltham, MA, USA) and 50 units/mL penicillin / 50 µg/mL streptomycin sulfate (#15,140,122, Gibco, Thermo Fisher Scientific, Waltham, MA, USA). LTED cells were cultivated in DMEM (w/o phenol red, #31,053,028), 10% charcoal-stripped FBS (#12,676,029, Gibco, Thermo Fisher Scientific, Waltham, MA, USA), 1 mM sodium pyruvate (#11,360,070, Gibco, Thermo Fisher Scientific, Waltham, MA, USA), 2 mM L-glutamine (#25,030,081, all Gibco, Thermo Fisher Scientific, Waltham, MA, USA) and 50 units/mL penicillin / 50 µg/mL streptomycin sulfate (#15,140,122, Gibco, Thermo Fisher Scientific, Waltham, MA, USA). After eight days of cultivation in respective media, cells were labeled using Hoechst-33342 (#62,249, Thermo Fisher Scientific, Waltham, MA, USA). Imaging of the plates was conducted with an IXM XLS microscope (Molecular Devices, San Jose, CA, USA). Image analysis was performed using the Molecular Devices Analysis Software, MetaXpress. Here, nuclei were detected based on the size and intensity of fluorescence in the DAPI channel, automatically counted. To investigate the impact of glutamine deprivation, the same media as above was used, however, either with or without glutamine supplementation. In conditions with glutamine, various final concentrations of glutamine were applied. Plates were incubated for eight days and then imaged as described above. Data was normalized to the 2 mM L-glutamine control.

siRNA and plasmid transfection

RNAi knockdown was accomplished with pools of siRNAs (*GLYATL1* (#si-G020—92,292), *ESR1* (#si-G020-2099), both from siTOOLs Biotech, Martinsried, Germany). Untarget Control siPools negC-120 (#si-C002; siTOOLs Biotech, Martinsried, Germany) served as a negative control. Cells were transfected using RNAiMAX® (Thermo Fisher Scientific, Waltham, MA, USA) according to the manufacturer's instructions and with 3 nM of siRNA. Transfected cells were analyzed by RT-qPCR 72 h post-transfection to assess knockdown efficiency (see below). Plasmids were transiently transfected into MCF7 and T47D cell lines with 2500 ng plasmid DNA and using 6 µL Lipofectamine™ 2000 (Thermo Fisher Scientific, Waltham, MA, USA), according to the manufacturer's instructions. HEK293FT cells were transiently transfected using plasmid DNA and linear polyethylenimine MW 25000 (PEI, #23,966, Polysciences, Warrington, PA, USA) as transfection reagent. HEK293FT cells were first trypsinized and subsequently seeded at a density of 1.5×10^6 cells in 9 mL of fresh growth medium. 4 µg plasmid DNA with 20 µL PEI (1 mg/mL) were mixed and incubated for 15 min at room temperature to allow the formation of DNA-PEI complexes. Following the incubation period, the transfection mixture was added dropwise to the prediluted cell suspension and plated on a 100 mm dish. After 24 h of transfection, the culture medium was replaced with fresh growth medium.

RT-qPCR

RNA was isolated using the RNeasy Mini Kit (#74,104, Qiagen, Hilden, Germany) with on-column DNA digestion, according to the manufacturer's instructions. Purified RNA was reverse transcribed utilizing the RevertAid RT Reverse Transcription Kit (#K1691, Thermo Fisher Scientific, Waltham, MA, USA) according to the manufacturer's instructions. Quantitative PCR was conducted using the Power SYBR Green PCR Master Mix (#4,368,706, Thermo Fisher Scientific, Waltham, MA,

USA), along with the QuantStudio™ 5 Real-Time PCR System (Thermo Fisher Scientific, Waltham, MA, USA). Data was analyzed utilizing the QuantStudio™ Design & Analysis Software v1.5.0. Relative changes in gene expression were determined using the comparative Ct (ΔΔCt) method [43] and visualized as $2^{-\Delta\Delta Ct}$. The median Ct values of technical replicates and the mean Ct values of biological replicates were used as basis for the ΔΔCt method and expression of the genes of interest was normalized to *ACTB* and *PUM1* housekeeping genes. The following primer pairs were used: *ACTB* forward 5′-ATTGGCAATGAGCGGTTC-3′, reverse 5′-GGATGCCACAGGACTCCA-3′; *PUM1* forward 5′-TCACATGGATCCTCTTCAAGC-3′, reverse 5′-CCTGGAGCAGCAGAGATGTAT-3′; *ESR1* forward 5′-GATGGGCTTACTGACCAACC-3′, reverse 5′-AAAGCCTGGCACCCTCTT-3′; *GLYATL1* forward 5′-CACATCAATCACGGGAACC-3′, reverse 5′-CCATGTCATCAGTCATCTCCTG-3′.

Transcription factor activity and pathway analysis

Differential gene expression analysis based on RNA-sequencing data was performed using the R package limma [44]. The resulting t-statistics values were used as input for the decoupleR R package [45] (version 2.8.0) to estimate transcription factor activities, which were based on the DoRothEA (v1.16.0) [46, 47] database containing signed and confidence-weighted TF–target gene-interactions.

Gene Set Enrichment Analysis (GSEA) [48] was performed with RNA-sequencing data using R package GSEA v4.1.0 (Build 27), while ReactomePA (version 1.46.0) [49] was used for gene set enrichment analysis in proteomic data, based on Reactome molecular pathways [50].

Patient data analysis

GEO datasets (GSE55374 [51], GSE10281 [52]) were used to assess *GLYATL1* expression in ER + breast cancer patients pretreated and after neoadjuvant therapy with 2.5 mg/day of the aromatase inhibitor letrozole. Patient samples of dataset GSE55374 had been profiled on Illumina HT-12v4 (*GLYATL1* probe: ILMN_1769032) and patients in the GSE10281 cohort on Affymetrix Human Genome U133 Plus 2.0 Array (*GLYATL1* probe: 1562089_at). Data from The Cancer Genome Atlas (TCGA) [53] were utilized for patient survival analysis. Clinical and survival data were extracted from the Cancer Genome Atlas (TCGA) for Kaplan–Meier survival analysis as described previously [54]. Patients were filtered for PAM50 subtype 'luminal A' and sorted by *GLYATL1* expression levels. Patients with an expression level below the median expression were assigned to the 'low' group, patients with above-median expression to the 'high' group. Overall survival rates were visualized as Kaplan–Meier plots using GraphPad Prism (v. 10), and statistical significance between patient groups was analyzed using the log-rank (Mantel-Cox) test.

Results

GLYATL1 is upregulated in two cell line models of luminal endocrine therapy-resistance

Estrogen-independent MCF7 and T47D cell lines were generated by continuously depriving cells of estrogen in vitro for one year, thereby mimicking the effects of aromatase inhibition. This resulted in long-term estrogen-deprived (LTED) MCF7 and T47D cell lines that had regained proliferative capacities in estrogen-depleted media [20, 21]. To elucidate transcriptomic and epigenomic alterations associated with resistance to estrogen deprivation, we characterized MCF7 parental and LTED cells using RNA- as well as ATAC-sequencing. ATAC-sequencing peaks within ± 2 kbp of the transcription start sites (TSS) which were gained in resistant MCF7 LTED cells compared to their estrogen-dependent counterpart (i.e., parental), were associated with differentially expressed genes (Fig. 1A). *GLYATL1* was among the top ten upregulated genes in MCF7 LTED cells (log2FC 11.79; padj 4.79E-18, Supplementary Table 1) and the *GLYATL1*-promoter was among the top 1% of genomic loci with gains in chromatin accessibility (chr11:58,926,244—58,926,663: log2FC 2.4; FDR 7.59E-06, Supplementary Table 2) compared to parental cells (Fig. 1A). The upregulation of GLYATL1 in MCF7 LTED cells was validated at both RNA and protein levels (Fig. 1B), and a similar upregulation of GLYATL1 was observed also in T47D LTED cells (Supplementary Fig. 1A). Clinical relevance of these in vitro findings was supported by survival analysis of luminal A patients from the TCGA cohort [53], which showed that high *GLYATL1* expression in treatment-naïve tumors was significantly associated with a worse overall patient survival (Fig. 1C). Analysis of two patient datasets comparing transcriptomic profiles of matching pre-and post-treatment samples from luminal breast cancer patients revealed significant increases in *GLYATL1* expression upon neoadjuvant administration of the AI letrozole for 2 weeks (GSE55374 [51]) and 3 months (GSE10281 [52]) (Fig. 1D).

Hypothesizing that GLYATL1 contributes to the resistance of the LTED cells, we then examined whether perturbation of *GLYATL1* expression in LTED cells would affect their growth under anti-estrogen treatment. To this end, we first tested whether reducing *GLYATL1* gene expression through siRNA-mediated knockdown influenced cell growth rates. Transient knockdown of *GLYATL1* in MCF7 LTED (Supplementary Fig. 1B) as well as in T47D LTED (Supplementary Fig. 1C) cells resulted in a significant reduction in proliferation under

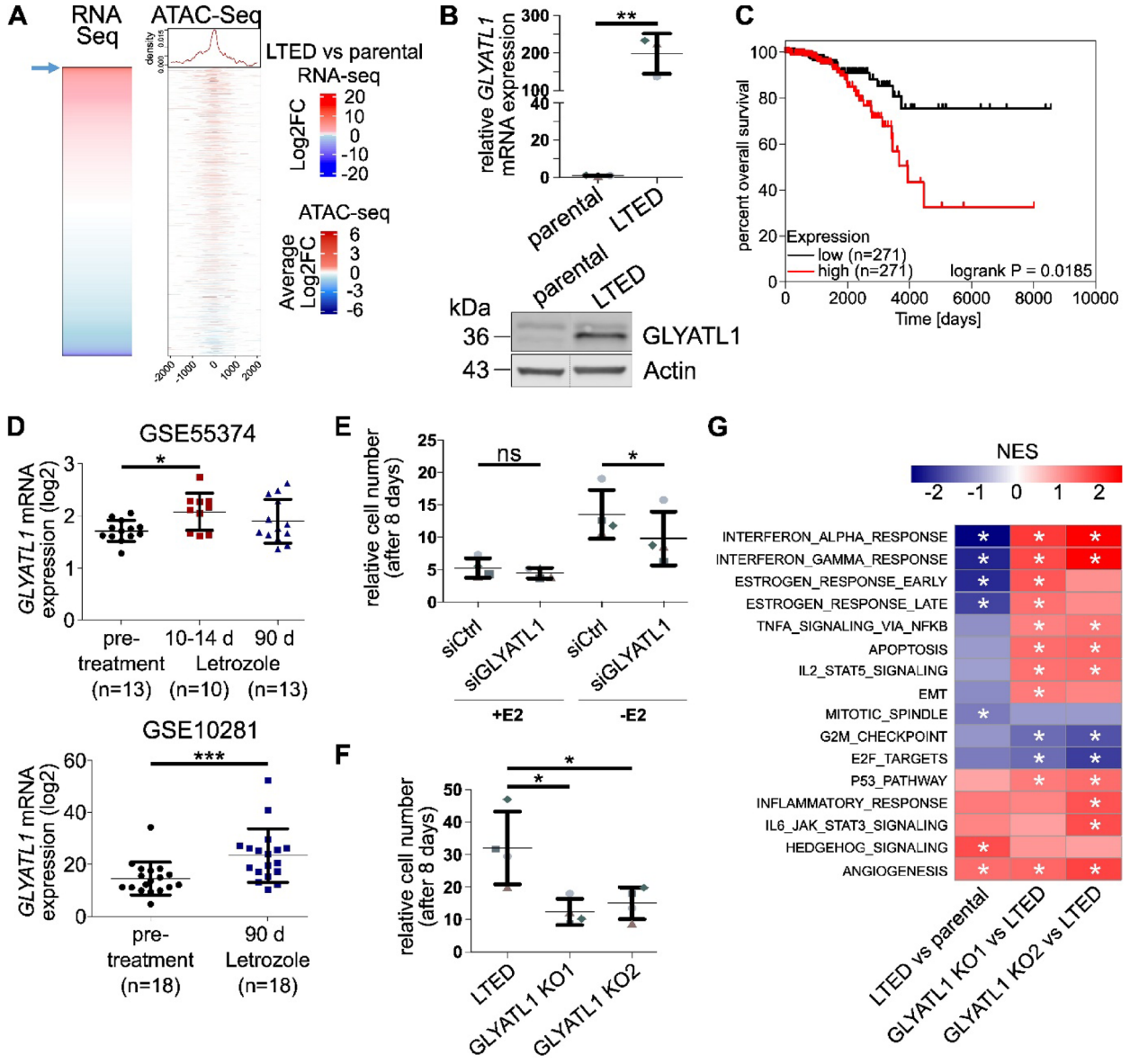

Fig. 1 (See legend on next page.)

estrogen-deprived conditions in both cell line models, but had no effect in the presence of estrogen (Fig. 1E, Supplementary Fig. 1D). This suggests a functional role of GLYATL1 in endocrine resistance. To validate these findings, we knocked out *GLYATL1* in MCF7 LTED cells and isolated two knockout (KO) clones (Supplementary Fig. 2). Of note, no viable *GLYATL1* KO cells could be obtained in the T47D cell line. Proliferation was significantly reduced in both MCF7 LTED *GLYATL1* knockout clones compared to the parental LTED cells (Fig. 1F), corroborating our results from *GLYATL1* knockdown. RNA-sequencing followed by Gene Set Enrichment Analysis (GSEA) [48] of the two LTED *GLYATL1* KO clones (Supplementary Table 3) revealed that several hallmark capabilities were altered in LTED compared to parental MCF7 cells; importantly, some of those were reversed when *GLYATL1* was knocked out in the LTED cells (Fig. 1G). As expected, expression of genes associated with ESTROGEN RESPONSE was strongly reduced in the LTED condition, which lacked estrogen in the media. Unexpectedly, this hallmark increased again in both LTED *GLYATL1* KO clones (Fig. 1G), although these cells were cultivated in media lacking estrogen. Assessment of *ESR1* transcript sequence reads in MCF7 parental and LTED cells, and the two LTED *GLYATL1* knockout clones did not reveal any pathogenic mutation in the *ESR1* gene that could be associated with resistance. Only a minor allele (c.1965G > A; p.T593 = relative to the reference sequence NM_001291241.2) having a low variant allele frequency in the parental MCF7 cell line (6%),

(See figure on previous page.)

Fig. 1 *GLYATL1* expression is associated with endocrine therapy and survival in patients, and with cell proliferation as well as estrogen independence in vitro. **A** Gene expression of MCF7 parental and long-term estrogen-deprived (LTED) cells was assessed by RNA-sequencing (n = 3) and differentially expressed genes were ranked by log2 fold change (log2FC). The rank position of *GLYATL1* in the heatmap is indicated by a blue arrow. Chromatin accessibility was analyzed by ATAC-sequencing (n = 2) in MCF7 parental and LTED cell lines, probing TSS ± 2 kb for long term estrogen deprived (LTED) compared to sensitive (i.e., parental) cells in the figure. Values represent summarized log2 fold changes across 40 bins around the TSS of each gene. The ATAC-seq heatmap is sorted in the same order of loci/genes as the heatmap from RNA-sequencing. **B** Expression of *GLYATL1* at mRNA and protein levels in parental and LTED MCF7 cell lines as detected by RT-qPCR (top) and Western blot (bottom), respectively. mRNA expression was normalized to *ACTB* and *PUM1* levels and relative changes to parental were calculated. Statistical significance was assessed using unpaired Student's t-test, ** indicates $p < 0.01$. Data are represented as the mean ± SEM (n = 3). Western Blot: β-actin was used as a loading control. Uncropped images of Western blots, data replication and validation of anti-GLYATL1 antibody are presented in the Supplementary File. **C** Median-based overall survival analysis of luminal A breast cancer patients in the TCGA dataset [53] of *GLYATL1* low (black) versus high (red) gene expression (n = 271 per group). Statistical significance was assessed using log-rank (Mantel-Cox) test using GraphPad Prism (v. 10). **D** GLYATL1 expression levels in two GEO datasets (GSE55374 [51], GSE10281 [52]) of matched tumor biopsies from ER + breast cancer patients before and after letrozole administration. Gene expression values are represented as log2 expression ± SD. Statistical significance was assessed using one-way ANOVA with Bonferroni post-test (GSE55374) or paired Student's t-test (GSE10281). * indicates $p < 0.05$, *** indicates $p < 0.001$. **E** Equal numbers of MCF7 LTED and LTED *GLYATL1* knockdown cells were cultivated in media with (+ E2) and without (-E2) 17-β-estradiol for 8 days. Cell numbers were then quantified via microscopy-based nuclear count and normalized to the seeding control. Statistical significance was assessed using paired Student's t-test. "ns" indicates a non-significant effect, * indicates $p < 0.05$. Data are presented as mean ± SEM (n = 4). **F***GLYATL1* was knocked out in MCF7 LTED cells, and proliferation rates of LTED cells and LTED *GLYATL1* knockout clones KO1 and KO2 were measured in media without estrogen via nuclear count, and normalized to the respective seeding control. Statistical significance was assessed using one-way ANOVA with Bonferroni post-test. * indicates $p < 0.05$. Data are presented as mean ± SEM (n = 4). **G** Geneset enrichment analysis of hallmark genes based on RNA-sequencing data from MCF7 parental and LTED cells, and the two LTED *GLYATL1* knockout clones KO1 and KO2 was performed using R package GSEA v4.1.0 (Build 27). Heatmap shows normalized enrichment scores (NES) for comparisons of LTED vs. parental cells and of LTED *GLYATL1* knockout clones KO1 and KO2 vs. LTED cells, respectively. The cut-off for statistical significance was set to a False Discovery Rate (FDR) q-value of < 0.25), and * indicates an FDR q < 0.25

was enriched in the LTED cells (49%) and in the two LTED GLYATL1 knockout clones (KO1: 40, KO2: 44%) (Supplementary Fig. 1E). The RNA-seq data further suggested that *ESR1* expression was strongly upregulated in LTED cells (log2FC 1.14, adj. *p*-value 0.0006; MS-proteomics: log2FC 3.40, adj. *p*-value 0.0295), and was even further increased specifically in *GLYATL1* knockout clone KO1, while *ESR1* expression was similar to LTED cells in clone KO2 (Supplementary Fig. 1E). Our findings thus indicate that GLYATL1 might affect ERα signaling, while it remains unclear if some direct feedback from GLYATL1 on expression of *ESR1* exists. Other hallmark capabilities showing consistent differences across conditions included INTERFERON-ALPHA- and INTERFERON-GAMMA-RESPONSE, while cell cycle-related hallmarks were negatively regulated in LTED cells, and even further downregulated in the two LTED *GLYATL1* KO clones (Fig. 1G). The latter is in agreement with the proliferation data shown in Fig. 1F.

Based on the RNA sequencing data, we next assessed transcription factor activities in MCF7 parental and LTED cells, and the two LTED *GLYATL1* knockout clones using the DoRothEA-decoupleR pipeline [45, 55]. Consistent with reduced proliferation of both MCF7 LTED *GLYATL1* knockout clones in estrogen-deprivation (Fig. 1F), activities of E2F1 and E2F4 were significantly repressed in the knockout clones (Supplementary Fig. 1F). Further, several transcription factors associated with stem cell-like activities (e.g., SOX2, PAX6, SNAI1,) were activated in MCF7 LTED cells, and this regulation was reversed in the LTED *GLYATL1* KO clones (Supplementary Fig. 1F). Concordant with GSEA, *ESR1*/ERα activity was reduced in the LTED condition compared to parental cells (Supplementary Fig. 1F, Supplementary Table 4). Yet, *ESR1* expression was upregulated in MCF7 and T47D LTED cells (Supplementary Fig. 1G), relative to their respective parental cell lines, potentially owing to compensatory feedback. Additionally, the activity of *ESR1*/ERα was further increased in LTED *GLYATL1* knockout clone KO1 relative to control LTED, while this was not evident in LTED *GLYATL1* clone KO2 (Fig. 1G). The latter findings are in accordance with the RNA-seq data (Supplementary Fig. 1E) and might implicate some relation between GLYATL1 and *ESR1*/ERα activity.

The observed differences between the two LTED *GLYATL1* knockout clones in some hallmark capabilities as well as in transcription factor activities prompted us to investigate whether the GLYATL1 protein was similarly depleted in the two LTED GLYATL1 knockout clones. Parallel reaction monitoring-based mass spectrometry of the MCF7 LTED *GLYATL1* KO clones showed different knockout levels of GLYATL1 at the protein level (Supplementary Fig. 1H, Supplementary Table 5). GLYATL1 protein levels were ~ 1% in LTED *GLYATL1* knockout clone KO1 but ~ 25% in clone KO2, compared to the parental LTED cells. No GLYATL1-peptides were reliably detected in the parental MCF7 cells, which was in line with a very high log2 foldchange difference between LTED vs. parental cells in the RNA-seq analysis (Supplementary Table 1). As a proliferation phenotype was observed also with *GLYATL1* knockout clone KO2, which showed a reduction of GLYATL1 protein by only 75%, GLYATL1 levels appear to be critical for growth and survival of therapy-resistant breast cancer cells, particularly under conditions of estrogen deprivation.

Having seen molecular (RNA-sequencing) and phenotypic differences between the two *GLYATL1* knockout clones we next characterized the CRISPR-induced aberrations. In both clones, a 454 bp deletion in one allele affected most of exon 3, including the start codon, and extended into intron 3 of the gene (Supplementary Fig. 2A). The alteration rendered this allele nonfunctional. A deletion of 20 bp in the second allele was upstream of the translation start and did not affect the reading frame. While *GLYATL1* knockout clones KO1 and KO2 shared the identical mutated alleles, they showed different extents of reduced read-coverage in exon 3 covering the start of the *GLYATL1* open reading frame, thus vastly reducing the amount of functional *GLYATL1* mRNA particularly in clone KO1 (Supplementary Fig. 2B,C). The alterations were reflected by aberrant splicing patterns that were particularly prominent in the KO1 clone as some canonical splicing of exon 3 to exon 4 was observed only in clone KO2 but not in KO1 (Supplementary Fig. 2C,D). Combined, this resulted in either reduced levels (clone KO2) or an almost complete loss (clone KO1) of GLYATL1- functional mRNA and protein (Supplementary Figs. 2D, 1H).

In summary, we found that *GLYATL1* expression increased in consequence of estrogen-deprivation in two independent in vitro models of endocrine resistance, was elevated also upon aromatase inhibitor therapy in patients, and correlated with poorer patient survival. In vitro, *GLYATL1* expression was required for proliferation of estrogen-deprived cells. Our findings suggest that GLYATL1 is associated with cell proliferation in luminal breast cancer under estrogen-deprived conditions and might affect ERα activity.

GLYATL1 expression is associated with succinate levels

We then performed quantitative proteomic analysis in the MCF7 parental, LTED and the two LTED *GLYATL1* knockout clones, to assess whether the effects of GLYATL1-expression were reflected also at the proteome level. While GLYATL1 was not detected in parental cells and in LTED *GLYATL1* knockout clone KO1, it was within the top 1% upregulated proteins in LTED compared to parental MCF7 cells (Supplementary Table 6), consistent with the results from PRM-analysis (Supplementary Fig. 1H). Principal component analysis of proteomic data revealed that the data obtained from the two knockout clones clustered away from both parental and LTED conditions (Supplementary Fig. 3A). A number of proteins were significantly upregulated in LTED compared to parental cells and downregulated in either one or both LTED *GLYATL1* knockout clones compared to LTED cells (Supplementary Fig. 3B, Supplementary Table 6). For example, ACSL3 and LEO1 were upregulated in LTED compared to parental cells and were strongly downregulated again in both LTED *GYLATL1* knockout clones (Supplementary Fig. 3C). ACSL3 activates long-chain fatty acids for synthesis of cellular lipids as well as for degradation via beta-oxidation [56], while LEO1 is a component of the PAF complex (PAF1C) and has been linked to epigenetic regulation of gene expression through histone modifications such as monoubiquitination of histone H2B and tri-methylation of H3K4 [57]. Congruent with the observed regulation of ACSL3, Reactome pathway analysis of the proteomic data revealed induction of lipid as well as of steroid metabolism and cholesterol biosynthesis in the LTED cells (Fig. 2A). Regulation of the latter is consistent with a previous report showing that 27-hydoxycholesterol can compensate for the lack of estrogen in MCF7 LTED cells [20]. Reduced protein levels of DNA polymerase epsilon (POLE) in the two knockout clones (Supplementary Fig. 3C) were in accordance with the lower proliferation rate (Fig. 1F) and with the downregulation of cell cycle activities in both LTED *GLYATL1* KO clones compared to their parental LTED cells (Fig. 1G). These results collectively demonstrate that GLYATL1 is critical for maintaining proliferation under endocrine therapy conditions in the two LTED cell line models, and its loss compromises fitness upon estrogen deprivation.

Reactome analysis of the proteomic data further suggested that the term 'TCA cycle and respiratory electron transport chain' was downregulated in LTED as compared to parental MCF7 cells, whereas it was significantly enriched in both LTED *GLYATL1* KO clones compared to LTED (Fig. 2A, Supplementary Table 7). While the log2 foldchange differences appeared to be minor for this Reactome term, down- and upregulation was consistent for the vast majority of enzymes mapping to the TCA cycle in the LTED and LTED *GLYATL1* KO clones, respectively (Fig. 2B).

Since Reactome pathway analysis suggested metabolic effects upon GLYATL1 perturbation, and because GLYATL1 is annotated also as a glutamine-*N*-acyltransferase [16], we hypothesized that its relevance upon estrogen-deprivation is associated with cellular metabolic homeostasis. Therefore, we next tested the effect glutamine limitation had on the viability of the MCF7 as well as T47D parental and LTED cell lines. Parental MCF7 cells were not affected by glutamine-restriction, while growth was moderately slowed down in the parental T47D cells (Fig. 2C). In contrast, proliferation of both LTED cell lines was strongly affected upon deprivation of glutamine (Fig. 2C) suggesting that LTED cells were addicted to glutamine. GLYATL1 and glutamine thus seemed to be essential in both endocrine resistant cell models. To uncover metabolic effects of GLYATL1 more comprehensively, we next quantified steady-state levels of intracellular soluble metabolites as well as N-acyl-CoA

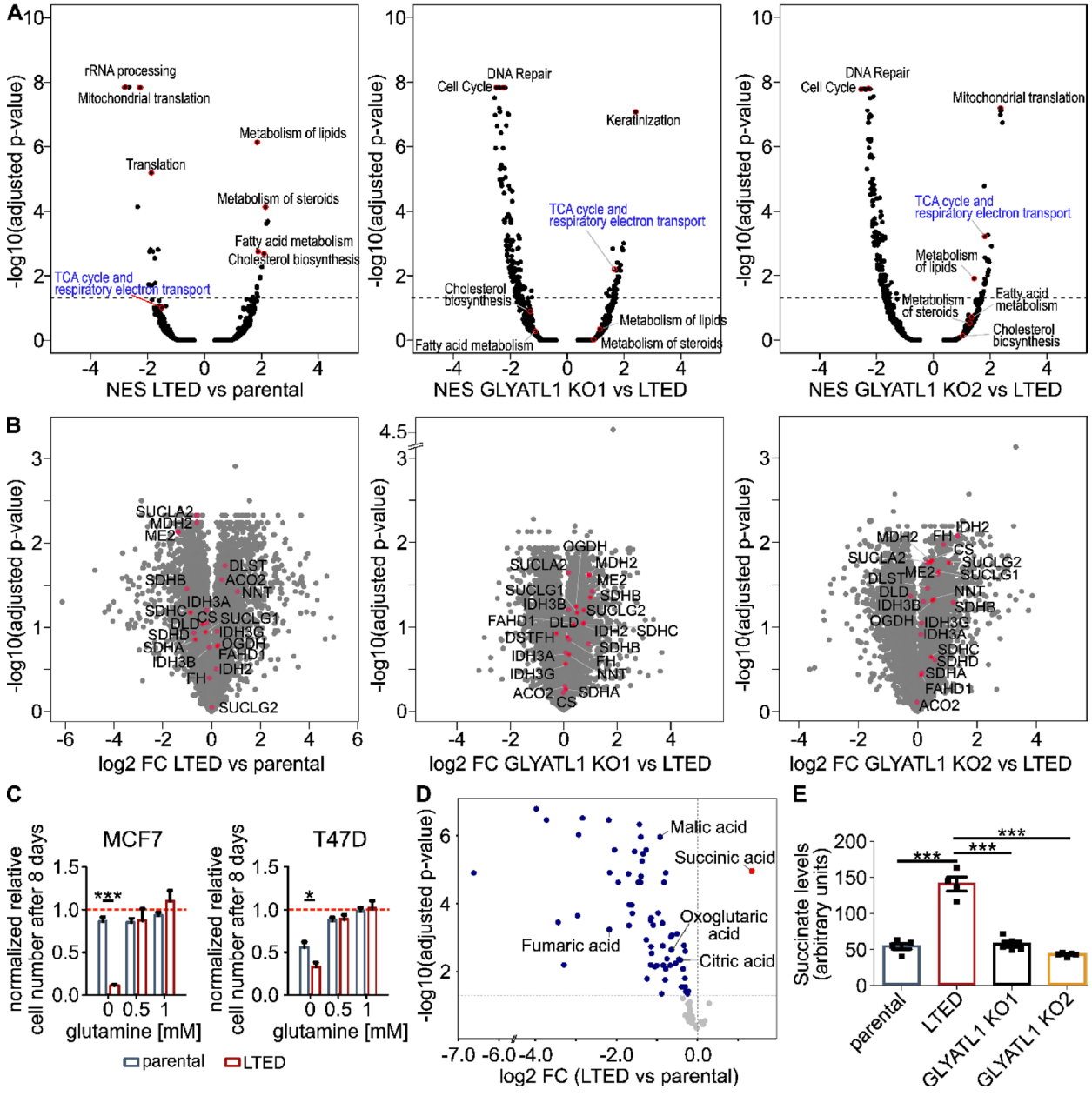

Fig. 2 GLYATL1-expression is associated with metabolic pathways and TCA cycle metabolites. **A** Log2 fold-changes of protein groups were calculated between the respective comparisons (n = 3) and sorted in decreasing order. Protein groups with duplicated gene names were removed and gene names were mapped to Entrez gene IDs based on the org.Hs.eg.db package (version 3.18.0) using the mapIds function of the AnnotationDbi package (version 1.65.1). The gsePathway function of the ReactomePA package (version 1.46.0) [49] was then applied to the sorted log2 fold-changes to perform gene set enrichment analysis based on Reactome molecular pathways [50]. Shown are the GSEA statistics (normalized enrichment scores (NES) and Benjamini–Hochberg adjusted *p*-values) for all Reactome pathways for the indicated comparisons. The term < TCA cycle and respiratory electron chain > is highlighted in the comparisons. **B** Volcano plots showing differential abundance (log2 fold changes (log2 FC)) of members of the Reactome pathway "TCA-cycle and respiratory electron chain" measured in a proteomic workflow between MCF7 LTED vs. parental cells and the two LTED *GLYATL1* knockout clones KO1 and KO2 vs. parental LTED cells, respectively. Differential protein expression was tested using unpaired Student's t-test followed by Benjamini–Hochberg adjustment of *p*-values. **C** MCF7 as well as T47D parental and LTED cell lines were cultivated for eight days in media with varying concentrations (0—2 mM) of glutamine. The proliferation rate was measured via microscopy-based nuclear counting. Proliferation was normalized to respective cells grown in 2 mM glutamine (dotted red line in the graphs). Statistical significance was assessed compared to the parental condition for every glutamine concentration individually using two-way ANOVA with Bonferroni post-test, *** indicates $p < 0.001$, * indicates $p < 0.05$. Insignificant differences are not indicated. Data are presented as mean ± SEM (n = 3 with 6 technical replicates each). **D** Steady-state levels of soluble metabolites were quantified in MCF7 parental and LTED by mass spectrometry (n ≥ 4). Colored dots represent metabolites with significantly higher (red) or lower (blue) steady-state levels. Quantified TCA intermediates are indicated. **E** Steady-state levels of succinate in MCF7 parental and LTED, and the two LTED *GLYATL1* knockout clones KO1 and KO2. Peak intensities were normalized by their respective internal standard and by protein levels. Statistical significance was assessed using one-way ANOVA with Bonferroni post-test, *** indicates $p < 0.001$. Data are presented as mean ± SEM of the biological replicates (n ≥ 4)

species in our set of MCF7 cell lines. Intracellular steady-state levels of glutamine and of glutathione were reduced in MCF7 LTED compared to the parental cells (Supplementary Fig. 4A, Supplementary Table 8) even though the genes encoding SLC38A1 and SLC38A2 glutamine transporters were upregulated in LTED cells (Supplementary Table 1) and the cells were routinely kept at high (2 mM) glutamine levels. Furthermore, and in agreement with the proteomic data, the steady-state levels of tricarboxylic acid cycle (TCA) intermediates, including the direct oxidation product of succinate (i.e., fumarate), the direct precursor of succinate (succinyl-CoA), and other TCA-metabolites were significantly downregulated in the LTED compared to parental MCF7 cells (Fig. 2D, Supplementary Fig. 4A,B, Supplementary Tables 8, 9). This was in line with a general downregulation of TCA cycle-associated genes in the LTED condition, which was partially reverted in the LTED *GLYALT1* KO clones (Supplementary Fig. 4C) and mostly in line with the different residual levels of GLYATL1 protein expressed in the two KO clones. The proteomic data matched these findings as the TCA-cycle proteins ME2, SDHB, SUCLA2 and MDH2 were among the most strongly downregulated proteins in the LTED vs. parental cells (Fig. 2B). Congruent with a potential role GLYATL1 might have in these alterations, TCA cycle-associated genes and proteins were elevated in LTED *GLYATL1* knockout cells, thus reversing the direction we had observed in the LTED cells (Fig. 2B, Supplementary Fig. 4C).

Succinate was the only TCA metabolite that had significantly higher steady-state levels in LTED cells while its levels were reversed back to the baseline in the two LTED *GLYATL1* knockout clones (Fig. 2 D,E, Supplementary Fig. 4A, Supplementary Table 8). This might be related, at least in part, to the reduced expression of *SDHB* [58] that we observed in LTED cells, and which was reverted in the two LTED *GLYATL1* knockout clones (Supplementary Fig. 4C). Of note, none of the TCA cycle genes that are recurrently mutated in cancer (i.e., *SDH*, *IDH*, *FH*) [59] were mutated in the MCF7 LTED cells or LTED *GLYATL1* knockout clones, as determined based on the RNA-seq data (not shown). Furthermore, there was also no indication of aberrant splicing of these genes in our RNA-sequencing data (not shown) that could have explained our observations. However, components of the 2-oxoglutarate dehydrogenase complex, *OGDH* and *DLD,* were strongly downregulated in the LTED cells, while *OGDH* was increased again in the two LTED *GLYATL1* KO clones (Supplementary Fig. 4C, Supplementary Tables 1, 3). The 2-oxoglutarate dehydrogenase complex catalyzes the conversion of 2-oxoglutarate to succinyl-CoA, a precursor of succinate. *OGDH*, as well as succinate, have previously been associated with cancer [60, 61]. Yet, the steady-state levels of 2-oxoglutarate and of succinyl-CoA were downregulated in the LTED and the LTED GLYATL1 knockout conditions (Supplementary Fig. 4A,B). Combined, these results suggest that GLYATL1 increases the steady state levels specifically of succinate in the MCF7 LTED cells, while the levels of the other TCA-cycle metabolites are likely not directly affected by GLYATL1. Of note, while LTED and *GLYATL1* knock out cells were cultivated in media supplemented with charcoal-stripped serum, parental cells were kept in media supplemented with FBS. Charcoal-stripping was necessary to deplete estrogen from the serum, however, this treatment removes also other components [62, 63]. Even though we observed reversal of some pathways (Fig. 2A), expression of TCA-cycle enzymes (Fig. 2B), and of succinate levels (Fig. 2E) in the knockout clones, we cannot exclude that some unknown component in serum, which is removed upon charcoal-stripping, might contribute to alterations we observed in the comparison of LTED vs. parental cells. Additional metabolic assays would be required to resolve this issue.

GLYATL1 is associated with epigenetic reprogramming

Succinate has been described as a competitive inhibitor of oxoglutarate-dependent dioxygenases, including lysine demethylases (KDMs) [62]. We thus hypothesized that GLYATL1 might impact the epigenetic landscape by modulating histone modifications via alteration of succinate levels. Along these lines, we next profiled the epigenetic landscape using Epigenetic-focused cytometry by Time-of-Flight (EpiTOF) [63, 64]. We measured signal intensities for target proteins and modifications across an average of approximately 40,500 single cells per condition (spread: 22,261 to 57,873 cells). Analysis of the resulting data indeed revealed consistent differences in histone mark abundance between parental, LTED, and LTED *GLYATL1* knockout cells (Fig. 3A, Supplementary Table 10). Specifically, H3K64ac and total histone H4 were significantly less abundant in parental MCF7 cells and the two LTED *GLYATL1* knockout clones as compared to LTED cells. A similar trend was observed for H3K4me3, which marks open chromatin [65], similarly to H3K64ac [66]. For H3K4me3, the EpiTOF pattern was consistent with the expression of LEO1 protein observed in our proteomic data (Supplementary Fig. 3B), as LEO1 is involved in the tri-methylation of histone H3K4 [57]. The H3K4me3-pattern matched also the increased steady-state level of succinate in LTED cells and the expression of *KDM5B* and *KDM5C* [65, 67], the latter two being increased in the LTED *GLYATL1* knockout clone KO1 compared to the LTED cells (Supplementary Fig. 5). H3K36me3, which has been described as a tumor suppressor mark [68], showed the reverse order, with lowest levels in the LTED cells (Fig. 3B). This pattern was in line with the expression of *KDM4D* (Supplementary

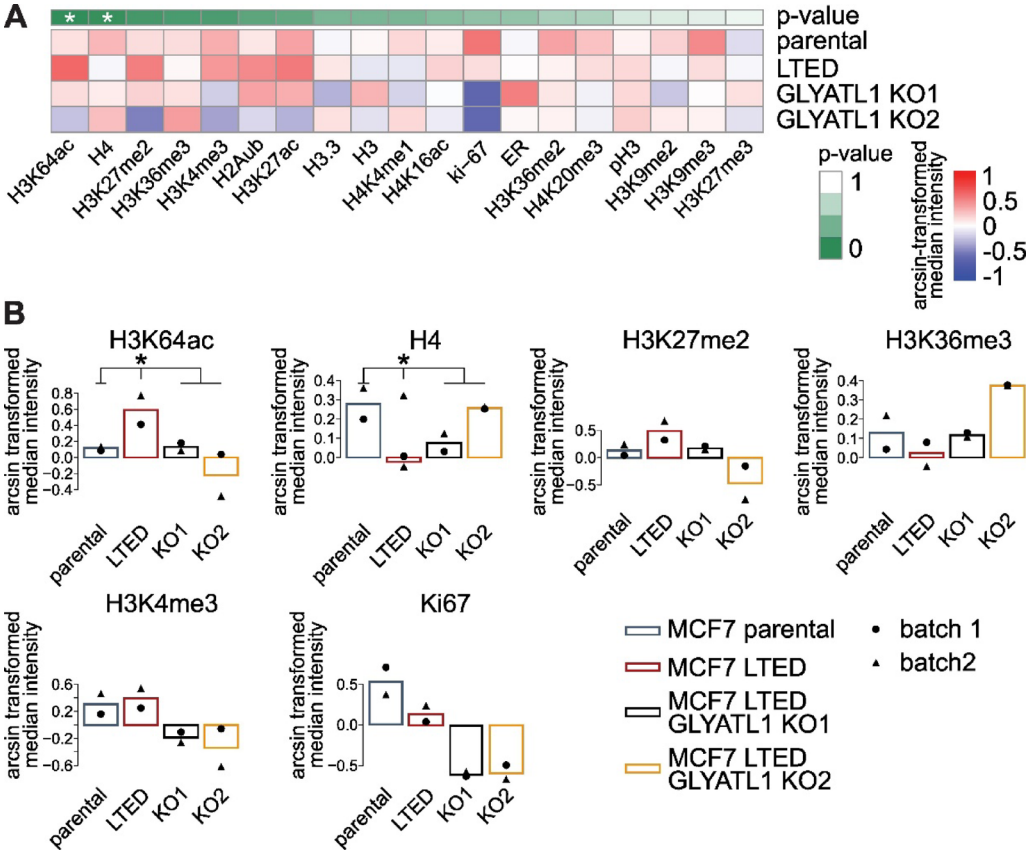

Fig. 3 GLYATL1 affects histone modifications. EpiTOF technology [63, 64] was applied to analyze epigenetic histone marks in MCF7 parental and long-term estrogen deprived (LTED) cells, and the two LTED *GLYATL1* knockout clones KO1 and KO2. **A** Data was arcsine transformed and normalized on core histones H3 and H3.3. For statistical comparison, median values of signal intensities were calculated for every condition. Using a two-sided, unpaired t-test, LTED was compared against the parental cells and both KO cells simultaneously. * indicates $p < 0.05$ **B** Two replicate experiments (filled triangles and circles, respectively) were performed. The means of the two replicates are indicated for modifications that reached significance or showed a consistent trend (e.g., upregulated in LTED compared to the parental cells and downregulated in the LTED *GLYATL1* KO clones compared to the LTED cells)

Fig. 5), which catalyzes H3K36me3 demethylation and which was most highly expressed in the LTED condition. These findings indicate that GLYATL1 may impact histone modifications via altered methylation and acetylation. However, further studies are warranted to fully uncover the functional effects of GLYATL1 on epigenetic regulation of chromatin. Of note, inclusion of Ki67 in the EpiTOF panel confirmed that Ki67 levels were congruent with the proliferation characteristics as well as with the results from GSEA of parental, LTED, and the two LTED *GLYATL1* knockout clones (compare Fig. 1 E,F), thus validating our approach.

As we had found GLYATL1 to be related to the mitochondrial TCA-cycle as well as to nuclear histone modifications, we next investigated the subcellular localization of GLYATL1 protein. Immunofluorescence staining indicated that recombinantly overexpressed GLYATL1 co-localized predominantly with mitochondria in MCF7 (Manders ' coefficient 0.861), T47D (Manders coefficient 0.467), as well as HEK293FT (Manders' coefficient 0.607) cells (Supplementary Fig. 6). These findings suggest that the epigenetic regulation that is associated with GLYATL1 is likely not direct, but potentially (also) via succinate. In conclusion, our findings suggest that GLYATL1 mediates alterations in cellular metabolism and epigenetic reprogramming, and these mechanisms may contribute to aromatase inhibitor resistance in luminal breast cancer.

Expression of GLYATL1 is regulated by estrogen-independent estrogen receptor activity

Having uncovered metabolic and epigenetic alterations that are associated with *GLYATL1*, we next aimed to understand how expression of this gene is regulated in the context of resistance to endocrine therapy. Gene set enrichment analysis had highlighted ERα signaling as a strongly downregulated pathway in LTED compared to parental cells (Fig. 1G). While loss of ERα activity was expected upon estrogen deprivation, ERα signaling appeared to be elevated in the LTED *GLYATL1* knockout cells (Fig. 1G). This observation indicated that ERα

signaling and *GLYATL1* expression might be interrelated. Hence, we next investigated this potential connection.

Consistent with previous findings [69], *ESR1* gene expression as well as ERα protein levels were upregulated in LTED compared to parental MCF7 cells (Supplementary Fig. 1G, Supplementary Tables 1, 6). However, this upregulation seemed to be independent of GLYATL1, as knockout of *GLYATL1* did not affect *ESR1*/ERα gene or protein expression (Supplementary Tables 3, 6). To uncover a potential relationship between ERα activity and *GLYATL1* expression, we next investigated how expression of the latter was regulated in the MCF7 parental and LTED cells.

In line with the findings described above (Fig. 1 A,B), genome-mapping of individual RNA-seq reads from MCF7 parental and LTED cells validated that *GLYATL1* was expressed only in the LTED but not the parental cells (Fig. 4A, Supplementary Fig. 2B). *GLYATL1* expression was induced mostly from the second annotated promoter of the gene, while there was no expression from either of the more distal and proximal promoters. Only in the LTED and not in parental MCF7, three ERα binding regions (MACS_peaks 3253-3255) were identified in ChIP-seq data (Fig. 4B) that had previously been generated using the same LTED cells we used in our study [20]. While MACS_peak 3253 mapped 30 kb upstream of the *GLYATL1* transcription start site, MACS_peaks 3254 and 3255 mapped < 1 kb proximal and distal of the transcription start site, respectively (Supplementary Fig. 7A,B). MACS_peak_3254 coincided with reduced DNA methylation and open chromatin (ATAC-seq) specifically in the LTED cells (Fig. 4C,D, Supplementary Fig. 7B-D). The reads from RNA-sequencing and the apparent presence of regulatory sequences matched RefSeq isoform 2 of *GLYATL1*, which is encoded by transcript variant 6 (NM_001389711.2) and is equivalent to ENSEMBL transcript ENST00000689150.1 (Fig. 4E, Supplementary Fig. 7E,F). The sequence at MACS_peak_3254 is annotated as a candidate proximal enhancer [70] (Supplementary Fig. 7G) and has been found (ENCODE data mapped in UCSC genome browser) to bind ERα, among other transcription factors (Supplementary Table 12). Distal MACS_peak_2355 mapped immediately upstream of an annotated lncRNA, however, chromatin was closed at this locus and no reads were sequenced that would suggest expression of that lncRNA (Supplementary Fig. 7A,B,D,E). Combined, our findings suggested that *GLYATL1* might potentially be regulated by ERα. However, this was in conflict with our results from Reactome and TF-activity analysis, which suggested that ERα signaling was rather downregulated in the LTED cells and was upregulated again in LTED *GLYATL1* knockout conditions (compare Fig. 1G, Supplementary Fig. 1F).

To resolve these contradicting observations, we next tested the effect estrogen has on *GLYATL1* expression in parental and LTED MCF7 cells. Parental MCF7 cells showed marginally increased *GLYATL1* expression when these cells were kept under estrogen deprivation for 48 h compared to cells grown in medium including estrogen, while the expression of *GLYATL1* was strongly reduced in LTED cells upon short time (i.e., 48 h) estrogen treatment (Fig. 4F). These findings were corroborated in T47D, where the same trend and significant regulation were observed, respectively (Supplementary Fig. 7H). Hence, negative regulation of *GLYATL1* expression appeared to be a rapid response to estrogen supplementation. We then tested if this negative effect of estrogen on *GLYATL1* expression would persist also for a longer time. To that end, we cultivated MCF7 and T47D LTED cells for three months in media either with or without estrogen. *GLYATL1* expression was indeed consistently reduced in MCF7 LTED cells grown in full medium with continuous presence of estrogen (Fig. 4G). After three months, we deprived the LTED cells of estrogen again and observed a significant increase in *GLYATL1* expression back to similar levels to those present in the original LTED cells (Fig. 4G). Consistent results were observed also in the T47D LTED cell line (Supplementary Fig. 7I), demonstrating that this dependency was not cell line-specific. Taken together, these results imply a strong and direct association between estrogen deprivation and *GLYATL1* expression, suggesting that *GLYATL1* is negatively regulated by estrogen and thus, putatively, also by estrogen-dependent ERα activity.

In light of these observations and the results from the analysis of ERα ChIP-seq data, we then knocked down *ESR1*/ERα in MCF7 and T47D LTED cells that were kept in estrogen-deprived media. Expression of *GLYATL1* was strongly reduced when ERα was depleted in MCF7 and in T47D LTED cells (Fig. 4H, Supplementary Fig. 7K), suggesting that *GLYATL1* expression was positively regulated by ERα, but only in the absence of estrogen. Accordingly, binding of ERα at the promoter of *GLYATL1* (MACS_peak_3254) coincided with open chromatin specifically in the MCF7 LTED cells (Fig. 4B,D, Supplementary Fig. 7B,D). Induction of ERα activity by ligands other than estrogen has been described before. In line with a report that had identified 27-hydroxycholesterol as a *bona fide* alternative regulator of ERα activity [20], expression of *CYP27A1*, which encodes the monooxygenase that converts cholesterol to 27-hydroxycholesterol, was upregulated in the MCF7 LTED cells compared to parental cells (log2FC 2.46, adjusted *p*-value 0.002). While CYP27A1 was not detected at the protein level, transcription factor activity analysis predicted activation of SREBF1 and SREBF2 in LTED cells (Supplementary Fig. 1F). These transcription factors, which regulate

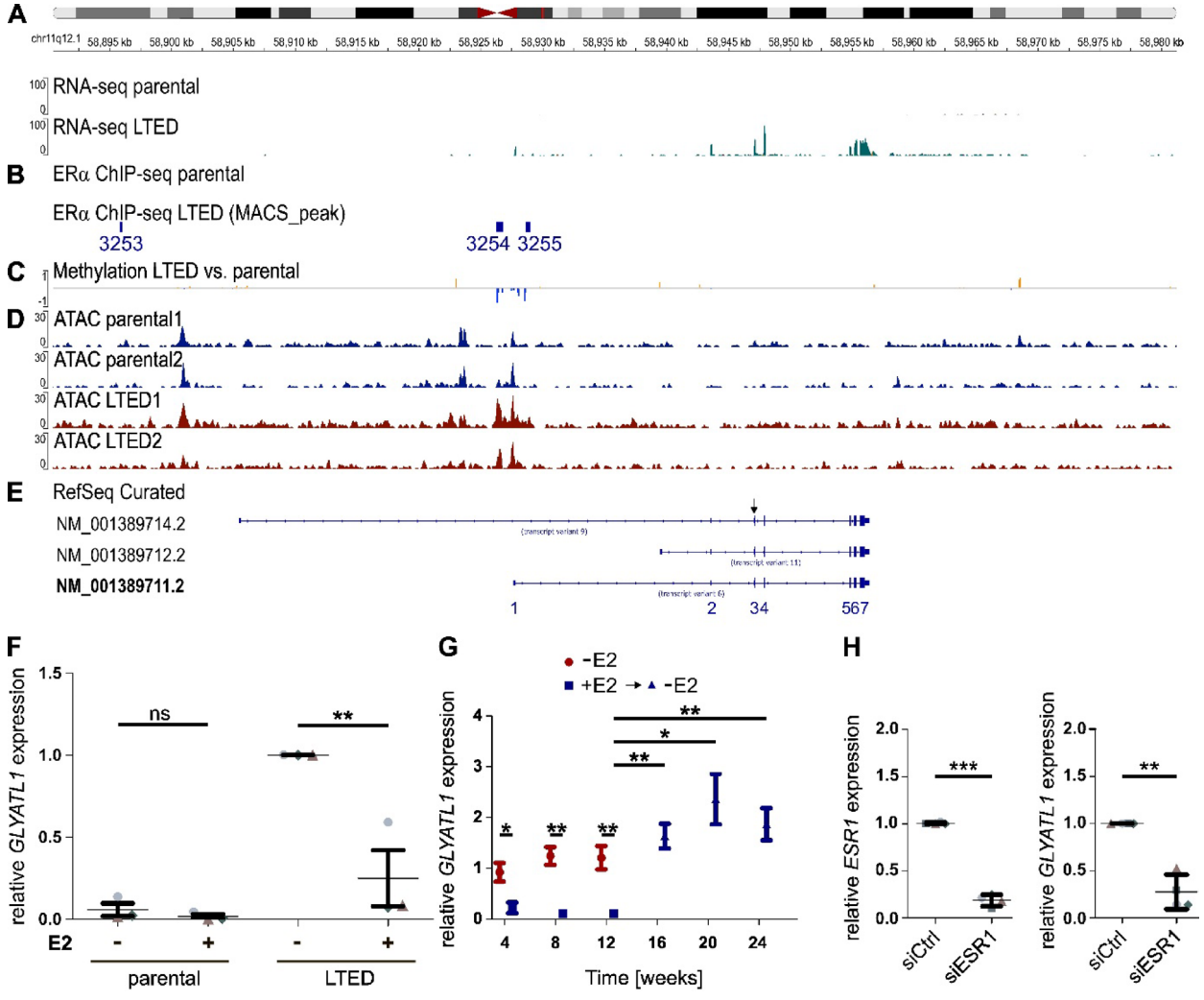

Fig. 4 *GLYATL1* expression is regulated by non-canonical estrogen-signaling in long term estrogen deprived MCF7 cells. A Zoom into the GLYATL1 gene locus (GRCh38/hg38) is shown with RNA-seq read-coverage (**A**), ERα ChIP-seq MACS_peaks (from GSE60517) (**B**), methylation changes (EPIC-array) (**C**), as well as ATAC-seq peaks, all acquired from MCF7 parental and long-term estrogen deprived (LTED) cell lines (**D**). Red and blue peaks in **C** depict hypermethylated and hypomethylated CpG positions in the LTED cells compared to parental MCF7, respectively. The RefSeq curated gene structure of *GLYATL1* and major transcript variants are indicated in (**E**). Note that all three variants encode the same protein (Accession number Q969I3 in UniProt), as translation starts in exon 3. The variant matching the RNA-seq peaks (compare panel A) is indicated in bold font and exons are numbered in this gene model. The mapping position of the sgRNA in exon 3 that was used to knockout *GLYATL1* (compare Methods and Supplementary Fig. 2) is indicated with an arrow. (F) Parental MCF7 cells (left) and MCF7 LTED cells (right) were cultivated for 48 h in their respective media without (-) or with (+) supplementation of 10 nM 17-β-estradiol (E2). Then, RNA was extracted and *GLYATL1* mRNA levels were assessed via RT-qPCR. Data from all conditions were normalized to LTED cells cultivated in estrogen-depleted media (n = 3, each with 3 technical replicates). Statistical significance was assessed using one-way ANOVA with Bonferroni post-test. ** indicates $p < 0.01$, ns: not significant. **G** MCF7 LTED cells were cultured in the presence (+ E2, blue squares) or absence (-E2, red circles) of 10 nM 17-β-estradiol for 12 weeks. Then, cells were deprived of estrogen again and cultivation was continued for another 12 weeks (+ E2—> -E2, black triangles). mRNA levels were determined by RT-qPCR from cultures harvested at the indicated time points. Relative changes to LTED cells cultivated in estrogen-deprived media were calculated (n ≥ 4, with 3 technical replicates each). Statistical significance was assessed using unpaired Student's t-tests. * indicates $p < 0.05$, ** indicates $p < 0.01$. **H** MCF7 LTED cells were transfected with non-targeting siRNA (siCtrl) or a pool of siRNAs targeting *ESR1* (siESR1) for 72 h. Knockdown efficiency (left) and effect on *GLYATL1* expression (right) were validated by RT-qPCR and relative levels with respect to control transfected cells were calculated. Values for mRNA expression were normalized to *ACTB* and *PUM1* expression levels. Statistical significance was assessed using paired Student's t-test, ** indicates $p < 0.01$, *** indicates $p < 0.001$. Data are represented by mean ± SEM (n = 3)

genes that are involved in cholesterol biosynthesis and lipid homeostasis [71], were the strongest downregulated TFs in the LTED *GLYATL1* KO1 clone (Supplementary Fig. 1F) which was devoid of GLYATL1 protein expression. Furthermore, cholesterol biosynthesis was significantly upregulated in the MCF7 LTED vs. parental cells, while this Reactome geneset was downregulated in LTED *GLYATL1* KO1 cells, supporting a potential involvement of GLYATL1 in the regulation of cholesterol biosynthesis (Fig. 2A). Collectively, these observations

indicate that *GLYALT1* expression can be induced by the estrogen receptor, but only in the absence of estrogen.

Finally, we tested if FOXA1 might be involved in the regulation of *GLYATL1* gene expression. FOXA1 is a pioneer factor required for binding of ERα to estrogen receptor regulated elements in the genome [72, 73] and binding of FOXA1 within MACS_peak_2354 has been found in several ChIP-seq datasets (Supplementary Table 12). To this end, we knocked down *FOXA1* in MCF7 and in T47D LTED cells (Supplementary Fig. 7L) and observed similar downregulation of *GLYATL1* expression (Supplementary Fig. 7 M) as we had seen upon knockdown of *ESR1* (Fig. 4H, Supplementary Fig. 7 K). Notably, *FOXA1* expression was not altered in LTED compared to parental MCF7 and T47D cells (Supplementary Fig. 7N), while *ESR1* expression was upregulated in LTED cells, in the absence of estrogen (Supplementary Fig. 1G). These findings show that *GLYATL1* gene expression is regulated by unconventional, i.e. estrogen-independent, ERα signaling in LTED conditions, which also requires FOXA1. Combined, this indicates that *GLYALT1*-expression indeed depends on ERα and FOXA1, however, is negatively affected by estrogen in two different long-term estrogen-deprived luminal breast cancer models. Taken together, our observations suggest that GLYATL1 and its activity support the ability of luminal breast cancer cells to overcome their dependency on estrogen [74].

Discussion

In the present study, we identify GLYATL1 as a novel player in the crossroads of metabolic and epigenetic mechanisms of resistance to estrogen deprivation, and provide insights into its regulation. GLYATL1 was strongly upregulated in two long term estrogen deprived (LTED) breast cancer cell line models mimicking aromatase inhibition, and perturbation of *GLYATL1* expression resulted in a significant proliferation disadvantage. As a proliferation-phenotype was observed also with *GLYATL1* knockout clone KO2, which showed a reduction of GLYATL1 protein by only 75%, GLYATL1 levels appear to be critical for growth and survival of therapy-resistant breast cancer cells, particularly under conditions of estrogen deprivation. GLYATL1 is annotated as an N-acyl-transferase family member that conjugates acyl groups to glutamine [16]. While we did not identify the particular substrate or product of the GLYATL1 enzymatic reaction, GLYATL1 was significantly associated with glutamine, as the viability of LTED cells was dependent on the supply of this amino acid. Furthermore, the steady-state levels of succinate were elevated in the MCF7 LTED model, while the levels of all other TCA cycle metabolites were reduced. GLYATL1 seemed to be relevant in this regulation as the levels specifically of succinate reverted back to baseline levels upon knockout of *GLYATL1* in the LTED cells. A complete loss of GLYATL1 protein seemed to be not required there as a reduction by 75% (*GLYATL1* knockout clone KO2 compared to LTED) sufficed to restore baseline succinate levels. Succinate has been implicated in tumor aggressiveness [61] and the LTED cells we employed in our study indeed showed elevated expression of stem-like marker genes and had shown increased metastatic potential in vitro and in vivo [20]. In contrast to succinate, several other metabolites (e.g., nucleosides and nucleotides, and a number of amino acids) were downregulated in the LTED condition. However, this seemed to be independent of GLYATL1, as their levels were unchanged in the LTED *GLYATL1* knockout clones. Yet, these observations are in agreement with the reduced proliferation potential we observed in LTED cells, which was even more prominent in the *GLYATL1* knockout clones. GLYATL1 thus seems to be an essential survival factor in our endocrine resistance model, and high GLYATL1 protein levels seem to be critical there.

Beyond its metabolic implications in the TCA cycle, succinate has been recognized as an onco-metabolite due to its ability to inhibit the activity of various oxoglutarate-dependent dioxygenases, key regulators of epigenetic modifications such as DNA methylation and histone modifications [62, 75]. Specifically, succinate can inhibit members of the histone demethylase family KDM, thereby influencing the methylation status of diverse histone residues [76]. In line with these findings, we observed increased levels of H3K4me3 in LTED cells. Elevated levels of this epigenetic mark have been reported to correlate with reduced progression-free survival and increased metastasis in breast cancer [77, 78]. Along the same lines, downregulation of H3K4me3 has been shown to enhance the response to the AI fulvestrant and reduce tumor growth and invasiveness by modulating cancer stemness [79]. These data align with increased activities of several transcription factors associated with stemness we found in the long-term estrogen deprived MCF7 cells, and with decreased H3K4me3 in the LTED *GLYATL1* knockout clones. H3K4me3 is targeted by KDM5 [65, 67], and we indeed observed reduced expression of *KDM5B* and *KDM5C* in the LTED compared to the parental cells, while expression of those histone demethylases was elevated in response to *GLYATL1* knockout.

In addition to these methylation marks, we observed alterations in acetylated histone residues, significantly for H3K64ac, which were elevated in LTED cells and diminished in response to *GLYATL1* perturbation. This mark defines transcriptionally active chromatin via regulation of nucleosome positioning at transcription start sites [66], and its downregulation in the *GLYATL1* knockout clones was in accordance with the reduced

activity of E2F1 and E2F4 transcription factors and the attenuated proliferative potential of these cells. Increased acetylation of H3K27, which did not reach significance in our EpiTOF analysis, was previously observed in the MCF7 LTED cells that we used in our study [20] and has been associated with endocrine therapy resistance in tamoxifen- and fulvestrant-resistant cells [80]. Elevated H3K27ac levels support resistance by promoting transcriptional activity, while inhibition of EP300/CREBBP, which catalyzes acetylation of H3K27, suppresses breast cancer growth in vitro and in vivo [77, 81].

Our findings further demonstrate that *GLYATL1* expression was negatively associated with estrogen availability, despite a positive association with ERα transcriptional activity. Analysis of chromatin immunoprecipitation sequencing (ChIP-seq) data [20] revealed direct ERα binding upstream of the *GLYATL1* transcription start site, exclusively in LTED cells. A few mechanisms have been reported for estrogen-independent activation of estrogen receptor signaling [82, 83]. For example, activation of ERα by IKKε (*IKBKE*) and DDX3X with an associated anti-viral response has been implicated with a potential link to endocrine resistance in luminal breast cancer [84]. However, while DDX3X was marginally upregulated in the LTED condition, IKKε was not changed and the associated interferon alpha and gamma responses were even reduced in LTED as compared to parental MCF7 cells (compare Fig. 1G). This suggests that this link is likely not relevant in our model. Upregulation of the estrogen receptor and estrogen-independent activity has been previously observed in the same LTED cells that we employed in our study [20]. There, this activation along with chromatin association and gene regulation had been attributed to the binding of 27-hydroxycholesterol to ERα and to epigenetic reprogramming [20]. In line with these findings, we observed 'cholesterol biosynthesis' and 'metabolism of steroids' as strongly upregulated gene sets in GSEA of transcriptomic data from LTED compared to parental cells. While canonical estrogen signaling was significantly downregulated in LTED compared to parental cells (compare Fig. 1G), our data suggests that estrogen receptor signaling that is independent of estrogen activates a distinct set of target genes, including *GLYATL1*.

In our initial prioritization of candidate factors for endocrine resistance, we had focused on GLYATL1 also because we observed a correlation between *GLYATL1* expression in clinical samples and the prognosis of breast cancer patients. The significant upregulation of *GLYATL1* expression in patient samples following letrozole treatment, coupled with its correlation with poor overall survival in ER-positive patients, supports its potential role in AI therapy resistance. Furthermore, estrogen-independent growth was associated with a dependence of tumor cells on glutamine in both cell line models and this could, at least in part [85], be related to the activity of GLYALT1. The dependency of LTED cells on glutamine and the correlation between the expression of *GLYATL1* and glutamine transporter *SLC38A1* in patients could thus suggest that GLYTL1 might be central in a mechanism that requires glutamine to overcome the negative impact of estrogen depletion on tumor cell viability upon aromatase inhibition. Glutamine addiction has been described as a therapeutic opportunity in cancer [86]. Targeting of glutaminase [87] might thus be a vulnerability also in progressing GLYATL1-high endocrine breast cancer.

Conclusions

In conclusion, we have identified GLYATL1 as a potential regulator of endocrine therapy resistance, particularly to aromatase inhibition, in ER + breast cancer. We have linked its activity to glutamine dependence, metabolic rewiring, and epigenetic reprogramming. There, GLYATL1 may contribute to transcriptional programs associated with endocrine therapy resistance by promoting succinate accumulation and influencing histone modifications. Targeting GLYATL1 and associated mechanisms might eventually be established as a treatment for AI-resistant luminal breast cancer.

Abbreviations

AI	Aromatase inhibitor
ATAC-seq	Assay for Transposase-Accessible Chromatin using sequencing
ChIP-seq	Chromatin immunoprecipitation sequencing
E2	Estrogen, 17-β-estradiol
EpiTOF	Epigenetic-focused cytometry by Time-of-Flight
ERα	Estrogen receptor alpha
ER+	Estrogen receptor (α) positive (breast cancer)
GLYATL1	Glycine-N-Acyltransferase Like 1
GSEA	Gene Set Enrichment Analysis
KDM	Lysine demethylase
KO	(CRISPR/Cas9) knock out
LTED	Long term estrogen deprived
TCA	Tricarboxylic acid cycle/citrate cycle

Supplementary Information

The online version contains supplementary material available at https://doi.org/10.1186/s13148-026-02133-w.

Supplementary Material 1. Supplementary Figure 1: GLYATL1 is upregulated in long time estrogen deprived (LTED) T47D cell line, and GLYALT1 expression correlates with patient survival as well as affects transcription factor activities. (A) Relative GLYATL1 mRNA expression in T47D parental and long-term estrogen-deprived (LTED) cell lines analyzed by RT-qPCR (left). mRNA expression was normalized to ACTB and PUM1 expression and relative changes to the parental cells were calculated. Data are represented as the mean ± SEM (n=3). Statistical significance was assessed using unpaired Student's t-test, *** indicates p<0.001. GLYATL1 protein levels in T47D parental and LTED cells was analyzed by Western Blot (right). β-actin was used as a loading control. Uncropped images of blots are presented in the Supplementary File. (B) GLYATL1 was knocked down via RNA interference in MCF7 LTED cells and knockdown verified via RT-qPCR, compared to MCF7 LTED cells transfected with a non-targeting control siRNA (siCtrl). Data are represented as the mean ± SEM (n=3). Statistical

significance was assessed using unpaired Student's t-test, *** indicates p<0.001. (C) GLYATL1 was knocked down via RNA interference in T47D LTED cells and knockdown verified via RT-qPCR, compared to T47D LTED cells transfected with a non-targeting control siRNA (siCtrl). Data are represented as the mean ± SEM (n=3). Statistical significance was assessed using unpaired Student's t-test, *** indicates p<0.001. (D) Equal numbers of T47D LTED control and LTED GLYATL1 knockdown cells were cultivated in media with (+E2) and without (-E2) estrogen for 8 days and cell numbers were then quantified via microscopy-based nuclear count and normalized to the respective seeding control. Statistical significance was assessed using paired Student's t-test. ns indicates non-significant p-value, * indicates p<0.05. (E) Read-coverage from RNA-sequencing in a window covering 63bp in the terminal exon of the ESR1 gene in MCF7 parental and LTED cells, and in LTED GLYATL1 knockout clones KO1 and KO2. A synonymous mutation (A-allele) relative to the G-allele in RefSeq reference sequence (NM_001385572.1) is highlighted. Read coverage and allele frequencies at this position are shown for all conditions. Graphics adapted from Integrative Genomics Viewer (IGV) [90]. (F) Relative transcription factor (TF) activities were estimated using DoRothEA [46, 47] R package. The heatmap visualizes TF activity scores in comparisons between MCF7 LTED vs. parental, and between the respective LTED GLYATL1 knockout clones (KO1 and KO2) vs. the LTED condition. TFs were filtered for an absolute(Score)>2 observed in any comparison. (G) RT-qPCR analysis of ESR1 expression in MCF7 and in T47D parental and long-term estrogen deprived (LTED) cell lines. Data are presented as mean ± SEM (n=3). Statistical significance was assessed using unpaired Student's t-test, ** indicates p<0.01. (H) Peak area of all GLYATL1 peptide (ALLLVTEDILK) fragment ions (indicated in color) in MCF7 parental and LTED, and LTED GLYATL1 knockout clones KO1 and KO2, determined by PRM-based targeted mass spectrometry. Data are represented as mean ± SEM (n=4). Statistical significance was assessed using unpaired Student's t-test based on the sum of all fragment ion intensities per samples, *** indicates $p<0.001$.

Supplementary Material 2. Supplementary Figure 2: Genotyping and assessment of coding potential of LTED GLYATL1 knockout clones. (A) Gene structure (hg38) of GLYATL1 (Reference transcript NM_001389711.2) and sequences in the stretch (red open box) covering the 5'-end of exon 3 up to sequence in intron 3 obtained by genotyping (Sanger sequencing) of purified PCR-products from parental, LTED, and GLYATL1 knockout clones KO1/KO2. Note: PCR products from two knockout alleles (Allele A, B) were sequenced individually, and sequences were identical in GLYATL1 knockout clones KO1 and KO2. Exonic sequence is indicated in upper case letters of nucleic acid sequence while intronic sequences are in lower case. Sequences deleted in respective knockout alleles within exon 3 and around the distal breakpoint within intron 3 are indicated by red dashes. Intermittent sequences not shown are indicated by dots (…). A five bp overlap of deleted sequence in alleles A and B is indicated by a black open box. The sequence and position of the sgRNA binding site is indicated in blue. The translation start of the GLYATL1 open reading frame is indicated and the encoded amino acid sequence is shown below the nucleotide sequences. (B) Read coverage from GLYATL1 RNA-sequencing data is shown for parental, LTED, and GLYATL1 knockout clones KO1 and KO2. No sequence reads were detected in the parental condition. A five bp sequence without read-coverage in GLYATL1 knockout clones KO1 and KO2 is indicated by a black open box. Intermittent regions not shown are indicated by dots (…). Graphics adapted from Integrative Genomics Viewer (IGV) [90]. (C) Inferred splice junction patterns supported by reads from RNA-sequencing of MCF7 parental, LTED, and LTED GLYATL1 knockout clones KO1 and KO2. Read counts supporting splicing from exon 3 to exon 4 are indicated in pink for LTED, GLATLY1 KO1 and KO2 clones. Graphics adapted from IGV [90]. (D) Read coverage and splice junctions in RNA-sequencing data obtained from parental, LTED, and LTED GLYATL1 knockout clones KO1 and KO2. Read counts supporting respective splice forms are indicated. Splicing of exon 2 to exon 3 (E2-E3) and of exon3 to exon 4 (E3-E4) indicates canonical splicing events of functional GLYATL1 transcripts, where splicing E3-E4 (indicated in pink) is critical for the coding potential of GLYATL1 mRNA. Splicing from exon 2 to exon 4 (E2-E4) indicates skipping of exon 3 and of the translational start of the GLYATL1 protein. Splicing from intron 3 to exon 4 (I3-E4) is indicative of transcription from allele A (545bp deletion), which lacks GLYATL1 coding potential. Results indicate that clone KO1 does not express functional GLYATL1 mRNA while expression of functional GLYATL1 mRNA is vastly reduced in clone KO2. These findings are reflected at the protein level (compare Supplementary Figure 1H.

Supplementary Material 3. Supplementary Figure 3: Proteomic changes associated with estrogen deprivation and with GLYATL1 protein expression. (A) Total proteins in MCF7 parental, long term estrogen deprived (LTED), and LTED GLYATL1 KO1 and KO2 cell lines were analyzed by mass spectrometry and protein intensities were used for principal component analysis. (B) VENN diagram depicting numbers of differentially expressed proteins, filtered for proteins significantly upregulated in MCF7 LTED vs. parental cells, and proteins significantly downregulated in MCF7 LTED GLYATL1 knockout clones KO1 or KO2 vs. LTED cells. Note: GLYATL1 is not listed as this protein was detected neither in parental nor in LTED GLYATL1 KO1 cells. Statistical significance was determined by Student's unpaired t-test and p-values were adjusted using the Benjamini-Hochberg method. Thresholds: log2FC >1 (LTED vs. parental) and <-1 (KO vs. LTED); significance: adjusted p-value < 0.05. (C) Hierarchically clustered heatmap showing z-scaled intensities of proteins with significant changes (adjusted p-values < 0.05) in LTED GLYATL1 KO1 and KO2 cell lines compared to parental or long-term estrogen deprived (LTED) MCF7 cell lines, with an absolute log2 fold-change of at least 1 in any comparison. Biological replicates (n=3) are displayed separately. Statistical significance was determined by Student's unpaired t-test and p-values were adjusted using the Benjamini-Hochberg method.

Supplementary Material 4. Supplementary Figure 4: Metabolomic analysis of MCF7 parental and long-term estrogen deprived (LTED) cells, and in LTED GLYATL1 knockout clones KO1 and KO2. (A) Hierarchical clustering showing z-scaled intensities, normalized by their respective internal standard levels, of soluble metabolites that were measured by mass spectrometry in MCF7 parental, LTED, and the LTED GLYATL1 knockout clones KO1 and KO2. Biological replicates (n≥4) are displayed individually. (B) Heatmap showing z-scaled values of acyl-CoA species measured via LC-MS in MCF7 parental and LTED cells, and two GLYATL1 knockout clones KO1 and KO2 (n=5). (C) Differential gene expression (RNA-sequencing) of indicated genes in the TCA-cycle as determined by DESeq2 analysis, sorted by their respective position in that cycle. Data extracted from Supplementary Tables 1 and 3. * indicates Benjamini-Hochberg adjusted p<0.05, ** indicates p<0.01, and *** indicates p<0.001.

Supplementary Material 5. Supplementary Figure 5: Differentially expressed methyltransferases and demethylases in MCF7 long-term estrogen deprived (LTED) vs. parental cells, and in LTED GLYATL1 knockout clones KO1 and KO2 vs. LTED cells. Heatmap displays log2 fold-changes (log2FC) in mRNA levels of genes encoding histone modifiers affecting methylation status as measured by RNA sequencing of MCF7 parental and long-term estrogen deprived (LTED) cells, and two LTED GLYATL1 knockout clones KO1 and KO2, followed by DESeq2 analysis. Respective comparisons are indicated below the heatmaps. Writers of histone marks are indicated in beige and erasers are indicated in green. Affected histone residues are indicated in colors for the respective epigenetic modifiers. * indicates Benjamini Hochberg adjusted p<0.05, ** indicates adjusted p<0.01, and *** indicates adjusted p<0.001.

Supplementary Material 6. Supplementary Figure 6: GLYATL1 protein localizes in the mitochondria in MCF7, T47D and HEK293FT cell lines. C-terminally FLAG-tagged GLYATL1 was recombinantly overexpressed in MCF7, T47D and HEK293FT cell lines by transient plasmid transfection. MCF7 and T47D cells were cultivated for 72 hours after transfection and HEK cells for 48 hours, and then incubated with abberior LIVE ORANGE dye to stain mitochondria (Mito). Cells were fixed and incubated with an anti-Flag antibody (FLAG) to detect the GLYATL1-FLAG fusion protein. Finally, nuclei were stained with DAPI and images taken using confocal immunofluorescence microscopy. Image analysis was performed using Zen Blue software and ImageJ (https://imagej.net/ij/). Representative images are shown. Scale bar = 10 µm.

Supplementary Material 7. Supplementary Figure 7: Regulation of GLYATL1 gene expression. Genomic mapping of regulatory sequence in the GLYATL1 gene locus (GRCh38/hg38) proximal and distal of the transcription start site. Shown is read coverage in RNA-seq data (A), data from ERα ChIP-seq (MACS_peaks from GSE60517 [20]) (B), methylation changes of LTED vs. parental condition (EPIC-array) (C), and ATAC-seq peaks acquired from MCF7 parental and long time estrogen-deprived

(LTED) cells (D). Gencode (E) and NCBI RefSeq (F) tracks from the UCSC genome browser mapping at the genomic region. (G) ENCODE4 Registry of candidate Cis-Regulatory Elements (cCREs) with putative enhancers indicated in yellow and putative promoters indicated in red. In (C), red and blue peaks depict hypermethylated and hypomethylated CpG positions, respectively, in the LTED cells compared to parental MCF7. Panels E-G have been adapted from the UCSC genome browser [22]. (H) Parental T47D cells (left) and T47D LTED cells (right) were cultivated for 48 hours in media without (-) or with (+) supplementation of 10 nM 17-β-estradiol (E2). Then, RNA was extracted and GLYATL1 mRNA levels were assessed via RT-qPCR. Data from all conditions were normalized to LTED cells cultivated in estrogen-depleted media (n=3, each with 3 technical replicates). Statistical significance was assessed using one-way ANOVA with Bonferroni post-test. ** indicates p<0.01, ns: not significant. (I) T47D LTED cells were cultured in the presence (+E2, blue squares) or absence (-E2, red circles) of estrogen for 12 weeks. After these initial 12 weeks, cells were deprived of estrogen again and cultivation was continued for another 12 weeks (+E2 -> -E2, black triangles). mRNA levels were determined by RT-qPCR from cultures harvested at the indicated time points. Relative changes to LTED cultivated in estrogen-deprived media were calculated (n≥4, with 3 technical replicates each). Statistical significance was assessed using unpaired Student's t-tests. * indicates p<0.05, ** indicates p<0.01. (K) T47D LTED cells were transfected with non-targeting siRNA (siCtrl) or a pool of siRNAs targeting ESR1 (siESR1) for 72h. Knockdown efficiency (left) and effect on GLYATL1 expression (right) were validated by RT-qPCR and relative levels with respect to control transfected cells were calculated. Values for mRNA expression were normalized to ACTB and PUM1 expression levels. Data are represented by mean ± SEM (n=3). Statistical significance was assessed using paired Student's t-test, * indicates p<0.05, *** indicates p<0.001. (L,M) MCF7 and T47D LTED cells were transfected with non-targeting siRNA (siCtrl) or a pool of siRNAs targeting FOXA1 (siFOXA1) for 72h. Knockdown efficiency (L) and effect on GLYATL1 expression (M) was assessed by RT-qPCR and relative levels with respect to control transfected cells were calculated. Values for mRNA expression were normalized to ACTB and PUM1 expression levels. Data are represented by mean ± SEM (n=3). Statistical significance was assessed using paired Student's t-test, * indicates p<0.05, *** indicates p<0.001. (N) Relative FOXA1 expression was analyzed in MCF7 and T47D parental and LTED cells. Values for mRNA expression were normalized to ACTB and PUM1 expression levels. Data are represented by mean ± SEM (n=3). Statistical significance was assessed using paired Student's t-test, ns indicates not significant difference.

Supplementary Material 8. Supplementary File: uncropped Western blots, validation of GLYATL1 antibody and initial validation of MCF7 LTED GLYATL1 knockout clones. Lysates from indicated MCF7 and T47D cell lines were separated by SDS-PAGE and blotted onto a PVDF membranes. The membranes were blocked for unspecific binding of proteins and then incubated with a primary anti GLYATL1 antibodies in blocking buffer. The next day, membranes were washed three times. Then, the blots were incubated with a secondary antibody, which was conjugated with Alexa Fluor™ 680, and washed again. Proteins were visualized with a LI-COR Odyssey scanner using 700 and 800 nm channels. Then, the same blots were reprobed with an anti ß-Actin antibody over night. The next day, the blots were washed and then incubated with a secondary antibody conjugated with DyLight™ 800 4X PEG. Protein bands were again visualized with a LI-COR Odyssey scanner using 700 and 800 nm channels. Original scans and accompanying files are provided in a supplementary ZIP-archive. (A) Cropped images (MCF7 from Figure 1B and T47D from Supplementary Figure 1A) are shown in the top left. The respective uncropped Western blot images of the original gel with indication of molecular weight markers (PageRuler Protein Ladder) are shown on the right. Samples from several MCF7 and T47D cell lines and derivatives were separated on the same gel. Lanes 2 and 4 (MCF7) and 7 and 9 (T47D) were cropped to generate the final images. Other conditions that were tested (i.e., TAMR and LTED-TAMR for MCF7 [20], TAMR for T47D [21]) were not regarded in the current study. (B) Protein lysates of indicated cell lines were generated on the indicated dates and analyzed by SDS-PAGE and Western blot. The same marker was used as in panel A. (C) Protein lysates from GLYATL1 knockout clones generated from MCF7 TAMR and LTED cells were tested for expression of GLYATL1 protein. Lysates from MCF7 TAMR and LTED cells were used as positive control for GLYATL1 expression. The same marker was used as in panel A.

Supplementary Material 9. Supplementary Table 1: Analysis of differentially expressed genes in RNA-sequencing data of MCF7 parental and long time estrogen deprived (LTED) cells. Gene expression levels (raw read counts from RNA-sequencing of MCF7 parental and LTED cells were used to identify differential gene expression employing DESeq2 v1.28.1 [29]. Indicated are log2 foldchanges and non-adjusted as well as FDR-adjusted p-values for all identified ENSEMBL/HGNC genes. Rawdata are available at GHGA (dataset ID: GHGAD23940263267179).

Supplementary Material 10. Supplementary Table 2: ATAC-sequencing of MCF7 parental and long-term estrogen deprived (LTED) cells. ATAC libraries were generated using a tagmentation protocol [31]. Sequencing reads were aligned to the hg38 reference genome and peaks were identified using MACS2 (v.2.2.9.1) [32]. Chromosomal coordinates of differentially accessible regions are annotated with log2 fold changes, non-adjusted P-values, and FDR adjusted p-values, each in comparisons of LTED and parental cells. Rawdata are available at GHGA (accession number: GHGAD24495022399035)

Supplementary Material 11. Supplementary Table 3: Analysis of differentially expressed genes in RNA-sequencing data of long-time estrogen deprived (LTED) cells and LTED GLYATL1 knockout clones KO1 and KO2. Gene expression levels (CPM) from RNA-sequencing of MCF7 LTED cells and LTED GLYATL1 knockout clones KO1 and KO2 were used to identify differential gene expression employing DESeq2 v1.28.1 [29]. Indicated are log2 foldchanges and non-adjusted as well as FDR-adjusted p-values for all identified ENSEMBL/HGNC genes. Results for comparison of GLYATL1 knockout clone KO1 vs. LTED are presented in sheet 1 of the table, while results for comparison of LTED GLYATL1 knockout clone KO2 vs. LTED are shown in sheet 2. Rawdata are available at GHGA (dataset ID: GHGAD23940263267179).

Supplementary Material 12. Supplementary Table 4: DoRothEA prediction of transcription factor activities in comparisons between MCF7 parental and long-term estrogen deprived (LTED) cells, and in LTED GLYATL1 knockout clones KO1 and KO2. Differential gene expression analysis was performed using RNA-sequencing data and the R package limma [44]. The resulting t-statistics values were used as input for the decoupleR R package [45] to estimate transcription factor activities, which were based on the DoRothEA (v1.16.0) [46, 47] database containing signed and confidence-weighted TF–target gene-interactions. Shown are DoRothEA scores and p-values for every comparison.

Supplementary Material 13. Supplementary Table 5: PRM based mass spectrometric analysis of GLYATL1 protein expression in MCF7 parental and long-term estrogen deprived (LTED) cells, and in LTED GLYATL1 knockout clones KO1 and KO2. The areas of the GLYATL1 fragment ions R.ALLLVTEDILK.L as measured in MS2 spectra from PRM mass spectrometry are indicated. Peak areas were computed by defining peak boundaries and summing up the areas of the fragment ions (n=4).

Supplementary Material 14. Supplementary Table 6: Proteomic analysis of in MCF7 parental and long-term estrogen deprived (LTED) cells, and in LTED GLYATL1 knockout clones KO1 and KO2. DIA mass spectrometry was applied to identify and quantify proteins in the indicated cell lines. Peptides and protein groups were identified using Spectronaut and quantified by summing up precursor signal areas under the curve. Shown are log2 transformed protein intensities for the different conditions and log2 fold-changes (FC) as well as Benjamini-Hochberg adjusted p-values (padj) for indicated comparisons (n=3). NA not detected. Rawdata are available via ProteomeXchange with identifier PXD067936.

Supplementary Material 15. Supplementary Table 7: Reactome analysis of proteomic data from MCF7 parental and long-term estrogen deprived (LTED) cells, and in LTED GLYATL1 knockout clones KO1 and KO2. Log2 fold-changes of protein groups were calculated between the respective comparisons (n=3) and sorted in decreasing order. Protein groups with duplicated gene names were removed and gene names were mapped to Entrez gene IDs based on the org.Hs.eg.db package (version 3.18.0) using the mapIds function of the AnnotationDbi package (version 1.65.1). The gsePathway function of the ReactomePA package (version 1.46.0) [49] was then applied to the sorted log2 fold-changes to perform gene set enrichment analysis based on Reactome molecular pathways [50]. Shown are

the GSEA statistics, including Benjamini-Hochberg adjusted p-values, for all Reactome pathways for the indicated comparisons.

Supplementary Material 16. Supplementary Table 8: Steady state levels of soluble metabolites measured in MCF7 parental and long-term estrogen deprived (LTED) cells, and in LTED GLYATL1 knockout clones KO1 and KO2. Indicated metabolites (with corresponding identifiers in the Human Metabolome Database – HMDB_ID) were quantified using mass spectrometry. Peaks corresponding to the calculated metabolite masses taken from an in-house metabolite library were integrated using the El-MAVEN software (https://docs.polly.elucidata.io/Apps/Metabolomic Data/El-MAVEN.html) and metabolite identification was supported by fragmentation patterns [41]. Peak intensities were normalized by their respective internal standard levels. Shown are peak intensities (C) of indicated conditions (n=5), mean intensities (MEAN) used for calculation of foldchanges (FC) as well as log2 fold changes (log2FC), and the p-values (pcal) and adjusted p-values (padj) of indicated comparisons.

Supplementary Material 17. Supplementary Table 9: Steady state levels of acyl-CoA species measured in MCF7 parental and long-term estrogen deprived (LTED) cells, and in LTED GLYATL1 knockout clones KO1 and KO2. Acyl-CoA species (Metabolite) were quantified using mass spectrometry. Peaks corresponding to the calculated metabolite masses taken from an in-house metabolite library were integrated using the El-MAVEN software (https://docs.polly.elucidata.io/Apps/Metabolomic Data/El-MAVEN.html) and acyl-CoA identification was supported by fragmentation patterns [40]. Peak intensities (C) were normalized by their respective internal standard levels. Shown are peak intensities of indicated conditions (n=5).

Supplementary Material 18. Supplementary Table 10: Median values from EpiTOF data measured in MCF7 parental, long-term estrogen deprived (LTED), and in LTED GLYATL1 knockout KO1 and KO2 cell lines. Median values from two replicate EpiTOF experiments of MCF7 parental, LTED, LTED GLYATL1 KO1 and KO2 conditions are shown for the indicated marks. Rawdata, i.e., z-scores for individual cells having been measured in the two replicates are available at Zenodo (https://doi.org/10.5281/zenodo.16947455).

Supplementary Material 19. Supplementary Table 11: List of primary antibodies used in EpiTOF analysis. Target specificities, conjugated elements and their isotopes, vendors, and order numbers (cat#) are indicated for antibodies that were used in EpiTOF profiling.

Supplementary Material 20. Supplementary Table 12: ReMap Atlas of Regulatory Regions annotated in UCSC genome browser at MACS_peak_2354. Data from the ReMap compendium [89] of public ChIP-seq dasets were downloaded from the ReMap ChIP-seq Track of the UCSC genome browser [22] at sequence where ERα ChIP-seq data from MCF7 LTED cells [20] mapped (i.e., MACS_peak_2354) upstream of the GLYATL1 transcription start site (Accessed: 28.01.2026).

Acknowledgements
We thank the DKFZ High-throughput DNA sequencing, OMICS Data IT, Microarray, Cellular Tools, Antibody, and Proteomics Core Facilities for performing excellent services. We thank Anke Heit-Mondrzyk for bioinformatics and Thomas Hielscher for statistical support. The results shown are in part, based upon data generated by the TCGA Research Network: (http://www.cancer.gov/tcga).

Author contributions
J.M., E.S. and S.W. conceived the study. J.M, E.S., Lu.S., Y.A., Li.S., S.O., C.S., S.B., A.W., S.K., D.H., R.W., I.H., and N.B.N, designed and performed in vitro experiments. Lu.S., E.W., K.K., S.O., B.E.M, V.R.d.M.C., C.S., P.L, and D.W. performed bioinformatic data analysis. J.M., E.S., Lu.S, and K.K. generated figures and tables. Y.Y., L.M., C.P., A.S., C.K, M.O., and S.W. supervised the study. J.M., Lu.S., C.K., and S.W. wrote the manuscript draft. All authors participated in discussions and interpretation of the data and results as well as read and approved the final manuscript.

Funding
Open Access funding enabled and organized by Projekt DEAL. This work was supported by the Cancer Transitional Research And EXchange Program (Cancer-TRAX) within the German–Israeli Helmholtz International Research School in Cancer Biology as well as by the European Union Horizon 2020 research and innovation program under the Marie Skłodowska-Curie grant agreement (EpiPredict–642691). The funding bodies played no role in the design of the study and collection, analysis, and interpretation of data and in writing the manuscript.

Availability of data and materials
OMICs datasets generated in the course of the current study are available in respective repositories: RNA-sequencing data of MCF7 parental, LTED, and LTED ***GLYTL1*** knockout clones KO1 and KO2 as well as ATAC-sequencing data of MCF7 parental and LTED cell lines are available at the GHGA Data Portal (https://data.ghga.de/) in the study GHGAS95686857321950 with accession numbers GHGAD23940263267179 (RNA-seq) and GHGAD24495022399035 (ATAC seq). EPIC 850 k methylome data of MCF7 parental and LTED cell lines are available at EMBL-EBI ArrayExpress database (https://www.ebi.ac.uk/biostudies/arrayexpress) with accession number E-MTAB-15519. Total DIA mass spectrometry proteomic data of MCF7 parental and LTED cells, and LTED ***GLYTL1*** knockout clones KO1 and KO2 have been deposited to the ProteomeXchange Consortium via the PRIDE [88] partner repository with the dataset identifier PXD067936. Raw EpiTOF data (i.e., z-scores for every mark measured in every cell) from MCF7 parental and LTED cells, and LTED ***GLYTL1*** knockout clones KO1 and KO2 are available at Zenodo (https://zenodo.org/) with record number 16947455 (https://doi.org/10.5281/zenodo.16947455). We re-analyzed the following datasets, which are available at public repositories: GEO datasets GSE55374 [51] and GSE10281 [52] are available from the Gene Expression Omnibus (https://www.ncbi.nlm.nih.gov/geo/). Breast cancer RNA-sequencing data [53] were downloaded from cBioPortal (https://www.cbioportal.org/). Other supporting data (Tables, Figures) are provided as Supplementary Information with the manuscript.

Declarations

Ethics approval and consent to participate
Not applicable.

Consent for publication
Not applicable.

Competing interests
The authors declare that they have no competing interests.

Author details
[1]Division of Molecular Genome Analysis, German Cancer Research Center (DKFZ), Im Neuenheimer Feld 580, 69120 Heidelberg, Germany
[2]Faculty of Biosciences, University of Heidelberg, Im Neuenheimer Feld 234, 69120 Heidelberg, Germany
[3]Department of Molecular Cell Biology, Weizmann Institute of Science, 76100 Rehovot, Israel
[4]G-INCPM, Weizmann Institute of Science, 76100 Rehovot, Israel
[5]Division of Tumor Metabolism and Microenvironment, German Cancer Research Center (DKFZ), Im Neuenheimer Feld 581, 69120 Heidelberg, Germany
[6]Division of Cancer Epigenomics, German Cancer Research Center (DKFZ), Im Neuenheimer Feld 280, 69120 Heidelberg, Germany
[7]Cellular Tools Core Facility, German Cancer Research Center (DKFZ), Im Neuenheimer Feld 580, 69120 Heidelberg, Germany
[8]Antibody Core Facility, German Cancer Research Center (DKFZ), Im Neuenheimer Feld 280, 69120 Heidelberg, Germany
[9]Department of Immunology and Regenerative Biology, Weizmann Institute of Science, 76100 Rehovot, Israel
[10]Present address: Bugworks Research Inc., Center for Cellular and Molecular Platforms, National Center for Biological Sciences, TIFR GKVK Campus, Bellary Road, Bangalore 560 065, India
[11]Department of Surgery and Cancer, Faculty of Medicine, Imperial College London, South Kensington Campus, London SW7 2AZ, UK
[12]Present address: Breast Epigenetic Plasticity and Evolution Group, The Institute of Cancer Research, 123 Old Brompton Road, London SW7 3RP, UK

Received: 17 October 2025 / Accepted: 7 April 2026
Published online: 29 April 2026

References

1. Bray F, Laversanne M, Sung H, Ferlay J, Siegel RL, Soerjomataram I, et al. Global cancer statistics 2022: GLOBOCAN estimates of incidence and mortality worldwide for 36 cancers in 185 countries. CA Cancer J Clin. 2024;74(3):229–63.
2. Siegel RL, Kratzer TB, Giaquinto AN, Sung H, Jemal A. Cancer statistics, 2025. CA Cancer J Clin. 2025;75(1):10–45.
3. Orrantia-Borunda E, Anchondo-Nunez P, Acuna-Aguilar LE, Gomez-Valles FO, Ramirez-Valdespino CA. Subtypes of Breast Cancer. In: Mayrovitz HN, editor. Breast Cancer. Brisbane (AU)2022.
4. Dunnwald LK, Rossing MA, Li CI. Hormone receptor status, tumor characteristics, and prognosis: a prospective cohort of breast cancer patients. Breast Cancer Res. 2007;9(1):R6.
5. Andrahennadi S, Sami A, Manna M, Pauls M, Ahmed S. Current landscape of targeted therapy in hormone receptor-positive and HER2-negative breast cancer. Curr Oncol. 2021;28(3):1803–22.
6. Pan H, Gray R, Braybrooke J, Davies C, Taylor C, McGale P, et al. 20-year risks of breast-cancer recurrence after stopping endocrine therapy at 5 years. N Engl J Med. 2017;377(19):1836–46.
7. Baselga J, Semiglazov V, van Dam P, Manikhas A, Bellet M, Mayordomo J, et al. Phase II randomized study of neoadjuvant everolimus plus letrozole compared with placebo plus letrozole in patients with estrogen receptor-positive breast cancer. J Clin Oncol. 2009;27(16):2630–7.
8. Bergamino MA, Morani G, Parker J, Schuster EF, Leal MF, Lopez-Knowles E, et al. Impact of duration of neoadjuvant aromatase inhibitors on molecular expression profiles in estrogen receptor-positive breast cancers. Clin Cancer Res. 2022;28(6):1217–28.
9. Li S, Shen D, Shao J, Crowder R, Liu W, Prat A, et al. Endocrine-therapy-resistant ESR1 variants revealed by genomic characterization of breast-cancer-derived xenografts. Cell Rep. 2013;4(6):1116–30.
10. Toy W, Shen Y, Won H, Green B, Sakr RA, Will M, et al. ESR1 ligand-binding domain mutations in hormone-resistant breast cancer. Nat Genet. 2013;45(12):1439–45.
11. Ahn S, Park JH, Grimm SL, Piyarathna DWB, Samanta T, Putluri V, et al. Metabolomic rewiring promotes endocrine therapy resistance in breast cancer. Cancer Res. 2024;84(2):291–304.
12. Achinger-Kawecka J, Stirzaker C, Portman N, Campbell E, Chia KM, Du Q, et al. The potential of epigenetic therapy to target the 3D epigenome in endocrine-resistant breast cancer. Nat Struct Mol Biol. 2024;31(3):498–512.
13. Magnani L, Stoeck A, Zhang X, Lanczky A, Mirabella AC, Wang TL, et al. Genome-wide reprogramming of the chromatin landscape underlies endocrine therapy resistance in breast cancer. Proc Natl Acad Sci USA. 2013;110(16):E1490–9.
14. Marusyk A, Janiszewska M, Polyak K. Intratumor heterogeneity: the Rosetta Stone of therapy resistance. Cancer Cell. 2020;37(4):471–84.
15. Beumers L, Vlachavas EI, Borgoni S, Schwarzmuller L, Penso-Dolfin L, Michels BE, et al. Clonal heterogeneity in ER+ breast cancer reveals the proteasome and PKC as potential therapeutic targets. NPJ Breast Cancer. 2023;9(1):97.
16. Matsuo M, Terai K, Kameda N, Matsumoto A, Kurokawa Y, Funase Y, et al. Designation of enzyme activity of glycine-N-acyltransferase family genes and depression of glycine-N-acyltransferase in human hepatocellular carcinoma. Biochem Biophys Res Commun. 2012;420(4):901–6.
17. Eich ML, Chandrashekar DS, Rodriguez Pen AM, Robinson AD, Siddiqui J, Daignault-Newton S, et al. Characterization of glycine-N-acyltransferase like 1 (GLYATL1) in prostate cancer. Prostate. 2019;79(14):1629–39.
18. Nalla AK, Williams TF, Collins CP, Rae DT, Trobridge GD. Lentiviral vector-mediated insertional mutagenesis screen identifies genes that influence androgen independent prostate cancer progression and predict clinical outcome. Mol Carcinog. 2016;55(11):1761–71.
19. Wang J, Shidfar A, Ivancic D, Ranjan M, Liu L, Choi MR, et al. Overexpression of lipid metabolism genes and PBX1 in the contralateral breasts of women with estrogen receptor-negative breast cancer. Int J Cancer. 2017;140(11):2484–97.
20. Nguyen VT, Barozzi I, Faronato M, Lombardo Y, Steel JH, Patel N, et al. Differential epigenetic reprogramming in response to specific endocrine therapies promotes cholesterol biosynthesis and cellular invasion. Nat Commun. 2015;6:10044.
21. Borgoni S, Sofyali E, Soleimani M, Wilhelm H, Muller-Decker K, Will R, et al. Time-resolved profiling reveals ATF3 as a novel mediator of endocrine resistance in breast cancer. Cancers (Basel). 2020;12(10).
22. Casper J, Speir ML, Raney BJ, Perez G, Nassar LR, Lee CM, et al. The UCSC Genome Browser database: 2026 update. Nucleic Acids Res. 2026;54(D1):D1331–5.
23. Heinz S, Benner C, Spann N, Bertolino E, Lin YC, Laslo P, et al. Simple combinations of lineage-determining transcription factors prime cis-regulatory elements required for macrophage and B cell identities. Mol Cell. 2010;38(4):576–89.
24. Langmead B, Salzberg SL. Fast gapped-read alignment with Bowtie 2. Nat Methods. 2012;9(4):357–9.
25. Li H, Handsaker B, Wysoker A, Fennell T, Ruan J, Homer N, et al. The Sequence Alignment/Map format and SAMtools. Bioinformatics. 2009;25(16):2078–9.
26. Tarasov A, Vilella AJ, Cuppen E, Nijman IJ, Prins P. Sambamba: fast processing of NGS alignment formats. Bioinformatics. 2015;31(12):2032–4.
27. Dobin A, Davis CA, Schlesinger F, Drenkow J, Zaleski C, Jha S, et al. STAR: ultrafast universal RNA-seq aligner. Bioinformatics. 2013;29(1):15–21.
28. Anders S, Pyl PT, Huber W. HTSeq--a Python framework to work with high-throughput sequencing data. Bioinformatics. 2015;31(2):166–9.
29. Love MI, Huber W, Anders S. Moderated estimation of fold change and dispersion for RNA-seq data with DESeq2. Genome Biol. 2014;15(12):550.
30. Ramirez F, Ryan DP, Gruning B, Bhardwaj V, Kilpert F, Richter AS, et al. deepTools2: a next generation web server for deep-sequencing data analysis. Nucleic Acids Res. 2016;44(W1):W160–5.
31. Buenrostro JD, Wu B, Chang HY, Greenleaf WJ. ATAC-seq: A Method for Assaying Chromatin Accessibility Genome-Wide. Current protocols in molecular biology / edited by Frederick M Ausubel [et al]. 2015;109:21 9 1- 9 9.
32. Zhang Y, Liu T, Meyer CA, Eeckhoute J, Johnson DS, Bernstein BE, et al. Model-based analysis of ChIP-Seq (MACS). Genome Biol. 2008;9(9):R137.
33. Robinson MD, McCarthy DJ, Smyth GK. edgeR: a Bioconductor package for differential expression analysis of digital gene expression data. Bioinformatics. 2010;26(1):139–40.
34. Zhu LJ, Gazin C, Lawson ND, Pages H, Lin SM, Lapointe DS, et al. ChIPpeakAnno: a Bioconductor package to annotate ChIP-seq and ChIP-chip data. BMC Bioinformatics. 2010;11:237.
35. Muller F, Scherer M, Assenov Y, Lutsik P, Walter J, Lengauer T, et al. RnBeads 2.0: comprehensive analysis of DNA methylation data. Genome Biol. 2019;20(1):55.
36. ORFeome Collaboration. The ORFeome Collaboration: a genome-scale human ORF-clone resource. Nat Methods. 2016;13(3):191–2.
37. Bolte S, Cordelieres FP. A guided tour into subcellular colocalization analysis in light microscopy. J Microsc. 2006;224(Pt 3):213–32.
38. Laemmli UK. Cleavage of structural proteins during the assembly of the head of bacteriophage T4. Nature. 1970;227(5259):680–5.
39. Benjamini Y, Hochberg Y. Controlling the false discovery rate - a practical and powerful approach to multiple testing. J R Stat Soc B Stat Methodol. 1995;57(1):289–300.
40. Agrawal S, Kumar S, Sehgal R, George S, Gupta R, Poddar S, et al. El-MAVEN: a fast, robust, and user-friendly mass spectrometry data processing engine for metabolomics. Methods Mol Biol. 2019;1978:301–21.
41. Bagwell CB, Inokuma M, Hunsberger B, Herbert D, Bray C, Hill B, et al. Automated data cleanup for mass cytometry. Cytometry A. 2020;97(2):184–98.
42. Nowicka M, Krieg C, Crowell HL, Weber LM, Hartmann FJ, Guglietta S, et al. CyTOF workflow: differential discovery in high-throughput high-dimensional cytometry datasets. F1000Res. 2017;6:748.
43. Livak KJ, Schmittgen TD. Analysis of relative gene expression data using real-time quantitative PCR and the 2(-Delta Delta C(T)) method. Methods. 2001;25(4):402–8.
44. Ritchie ME, Phipson B, Wu D, Hu Y, Law CW, Shi W, et al. limma powers differential expression analyses for RNA-sequencing and microarray studies. Nucleic Acids Res. 2015;43(7):e47.
45. Badia IMP, Velez Santiago J, Braunger J, Geiss C, Dimitrov D, Muller-Dott S, et al. decoupleR: ensemble of computational methods to infer biological activities from omics data. Bioinform Adv. 2022;2(1):vbac016.
46. Garcia-Alonso L, Holland CH, Ibrahim MM, Turei D, Saez-Rodriguez J. Benchmark and integration of resources for the estimation of human transcription factor activities. Genome Res. 2019;29(8):1363–75.
47. Muller-Dott S, Tsirvouli E, Vazquez M, Ramirez Flores RO, Badia IMP, Fallegger R, et al. Expanding the coverage of regulons from high-confidence prior knowledge for accurate estimation of transcription factor activities. Nucleic Acids Res. 2023;51(20):10934–49.
48. Subramanian A, Tamayo P, Mootha VK, Mukherjee S, Ebert BL, Gillette MA, et al. Gene set enrichment analysis: a knowledge-based approach for interpreting genome-wide expression profiles. Proc Natl Acad Sci U S A. 2005;102(43):15545–50.
49. Yu G, He QY. ReactomePA: an R/Bioconductor package for reactome pathway analysis and visualization. Mol Biosyst. 2016;12(2):477–9.

50. Milacic M, Beavers D, Conley P, Gong C, Gillespie M, Griss J, et al. The reactome pathway knowledgebase 2024. Nucleic Acids Res. 2024;52(D1):D672–8.
51. Arthur LM, Turnbull AK, Webber VL, Larionov AA, Renshaw L, Kay C, et al. Molecular changes in lobular breast cancers in response to endocrine therapy. Cancer Res. 2014;74(19):5371–6.
52. Creighton CJ, Li X, Landis M, Dixon JM, Neumeister VM, Sjolund A, et al. Residual breast cancers after conventional therapy display mesenchymal as well as tumor-initiating features. Proc Natl Acad Sci U S A. 2009;106(33):13820–5.
53. Cancer Genome Atlas N. Comprehensive molecular portraits of human breast tumours. Nature. 2012;490(7418):61–70.
54. Li X, Michels BE, Tosun OE, Jung J, Kappes J, Ibing S, et al. 5'isomiR-183-5p|+2 elicits tumor suppressor activity in a negative feedback loop with E2F1. J Exp Clin Cancer Res. 2022;41(1):190.
55. Holland CH, Tanevski J, Perales-Paton J, Gleixner J, Kumar MP, Mereu E, et al. Robustness and applicability of transcription factor and pathway analysis tools on single-cell RNA-seq data. Genome Biol. 2020;21(1):36.
56. Bu SY, Mashek MT, Mashek DG. Suppression of long chain acyl-CoA synthetase 3 decreases hepatic de novo fatty acid synthesis through decreased transcriptional activity. J Biol Chem. 2009;284(44):30474–83.
57. Rozenblatt-Rosen O, Hughes CM, Nannepaga SJ, Shanmugam KS, Copeland TD, Guszczynski T, et al. The parafibromin tumor suppressor protein is part of a human Paf1 complex. Mol Cell Biol. 2005;25(2):612–20.
58. Dalla Pozza E, Dando I, Pacchiana R, Liboi E, Scupoli MT, Donadelli M, et al. Regulation of succinate dehydrogenase and role of succinate in cancer. Semin Cell Dev Biol. 2020;98:4–14.
59. Laurenti G, Tennant DA. Isocitrate dehydrogenase (IDH), succinate dehydrogenase (SDH), fumarate hydratase (FH): three players for one phenotype in cancer? Biochem Soc Trans. 2016;44(4):1111–6.
60. Burr SP, Costa AS, Grice GL, Timms RT, Lobb IT, Freisinger P, et al. Mitochondrial protein lipoylation and the 2-oxoglutarate dehydrogenase complex controls hif1alpha stability in aerobic conditions. Cell Metab. 2016;24(5):740–52.
61. Kuo CC, Wu JY, Wu KK. Cancer-derived extracellular succinate: a driver of cancer metastasis. J Biomed Sci. 2022;29(1):93.
62. Xiao M, Yang H, Xu W, Ma S, Lin H, Zhu H, et al. Inhibition of alpha-KG-dependent histone and DNA demethylases by fumarate and succinate that are accumulated in mutations of FH and SDH tumor suppressors. Genes Dev. 2012;26(12):1326–38.
63. Aylon Y, Furth N, Mallel G, Friedlander G, Nataraj NB, Dong M, et al. Breast cancer plasticity is restricted by a LATS1-NCOR1 repressive axis. Nat Commun. 2022;13(1):7199.
64. Harpaz N, Mittelman T, Beresh O, Griess O, Furth N, Salame TM, et al. Single-cell epigenetic analysis reveals principles of chromatin states in H33–K27M gliomas. Mol Cell. 2022;82(14):2696–713.
65. Wang H, Fan Z, Shliaha PV, Miele M, Hendrickson RC, Jiang X, et al. H3K4me3 regulates RNA polymerase II promoter-proximal pause-release. Nature. 2023;615(7951):339–48.
66. Di Cerbo V, Mohn F, Ryan DP, Montellier E, Kacem S, Tropberger P, et al. Acetylation of histone H3 at lysine 64 regulates nucleosome dynamics and facilitates transcription. Elife. 2014;3:e01632.
67. Tumber A, Nuzzi A, Hookway ES, Hatch SB, Velupillai S, Johansson C, et al. Potent and selective KDM5 inhibitor stops cellular demethylation of H3K4me3 at transcription start sites and proliferation of MM1S myeloma cells. Cell Chem Biol. 2017;24(3):371–80.
68. Xiao C, Fan T, Tian H, Zheng Y, Zhou Z, Li S, et al. H3K36 trimethylation-mediated biological functions in cancer. Clin Epigenetics. 2021;13(1):199.
69. Kuske B, Naughton C, Moore K, Macleod KG, Miller WR, Clarke R, et al. Endocrine therapy resistance can be associated with high estrogen receptor alpha (ERalpha) expression and reduced ERalpha phosphorylation in breast cancer models. Endocr Relat Cancer. 2006;13(4):1121–33.
70. Moore JE, Pratt HE, Fan K, Phalke N, Fisher J, Elhajjajy SI, et al. An expanded registry of candidate cis-regulatory elements. Nature. 2026.
71. Amemiya-Kudo M, Shimano H, Hasty AH, Yahagi N, Yoshikawa T, Matsuzaka T, et al. Transcriptional activities of nuclear SREBP-1a, -1c, and -2 to different target promoters of lipogenic and cholesterogenic genes. J Lipid Res. 2002;43(8):1220–35.
72. Laganiere J, Deblois G, Lefebvre C, Bataille AR, Robert F, Giguere V. From the Cover: Location analysis of estrogen receptor alpha target promoters reveals that FOXA1 defines a domain of the estrogen response. Proc Natl Acad Sci USA. 2005;102(33):11651–6.
73. Hurtado A, Holmes KA, Ross-Innes CS, Schmidt D, Carroll JS. FOXA1 is a key determinant of estrogen receptor function and endocrine response. Nature Genet. 2011;43(1):27–33.
74. Lippman M, Bolan G, Huff K. The effects of estrogens and antiestrogens on hormone-responsive human breast cancer in long-term tissue culture. Cancer Res. 1976;36(12):4595–601.
75. Martinez-Reyes I, Chandel NS. Mitochondrial TCA cycle metabolites control physiology and disease. Nat Commun. 2020;11(1):102.
76. Laukka T, Myllykoski M, Looper RE, Koivunen P. Cancer-associated 2-oxoglutarate analogues modify histone methylation by inhibiting histone lysine demethylases. J Mol Biol. 2018;430(18 Pt B):3081–92.
77. Berger L, Kolben T, Meister S, Kolben TM, Schmoeckel E, Mayr D, et al. Expression of H3K4me3 and H3K9ac in breast cancer. J Cancer Res Clin Oncol. 2020;146(8):2017–27.
78. Messier TL, Gordon JA, Boyd JR, Tye CE, Browne G, Stein JL, et al. Histone H3 lysine 4 acetylation and methylation dynamics define breast cancer subtypes. Oncotarget. 2016;7(5):5094–109.
79. Kao HY, Pai CP, Wang H, Agarwal N, Adams J, Liu Z, et al. The PML1-WDR5 axis regulates H3K4me3 marks and promotes stemness of estrogen receptor-positive breast cancer. Res Sq. 2023.
80. Achinger-Kawecka J, Valdes-Mora F, Luu PL, Giles KA, Caldon CE, Qu W, et al. Epigenetic reprogramming at estrogen-receptor binding sites alters 3D chromatin landscape in endocrine-resistant breast cancer. Nat Commun. 2020;11(1):320.
81. Bommi-Reddy A, Park-Chouinard S, Mayhew DN, Terzo E, Hingway A, Steinbaugh MJ, et al. CREBBP/EP300 acetyltransferase inhibition disrupts FOXA1-bound enhancers to inhibit the proliferation of ER+ breast cancer cells. PLoS ONE. 2022;17(3):e0262378.
82. Jeng MH, Shupnik MA, Bender TP, Westin EH, Bandyopadhyay D, Kumar R, et al. Estrogen receptor expression and function in long-term estrogen-deprived human breast cancer cells. Endocrinology. 1998;139(10):4164–74.
83. Traphagen NA, Hosford SR, Jiang A, Marotti JD, Brauer BL, Demidenko E, et al. High Estrogen Receptor Alpha activation confers resistance to estrogen deprivation and is required for therapeutic response to estrogen in breast cancer. Oncogene. 2021;40(19):3408–21.
84. Pardeshi J, McCormack N, Gu L, Ryan CS, Schroder M. DDX3X functionally and physically interacts with Estrogen Receptor-alpha. Biochim Biophys Acta Gene Regul Mech. 2022;1865(2):194787.
85. Qiu Y, Stamatatos OT, Hu Q, Ruiter Swain J, Russo S, Sann A, et al. The unique catalytic properties of PSAT1 mediate metabolic adaptation to glutamine blockade. Nat Metab. 2024;6(8):1529–48.
86. Wise DR, Thompson CB. Glutamine addiction: a new therapeutic target in cancer. Trends Biochem Sci. 2010;35(8):427–33.
87. Lee CH, Motzer R, Emamekhoo H, Matrana M, Percent I, Hsieh JJ, et al. Telaglenastat plus Everolimus in advanced renal cell carcinoma: a randomized, double-blinded, placebo-controlled, Phase II ENTRATA trial. Clin Cancer Res. 2022;28(15):3248–55.
88. Perez-Riverol Y, Bandla C, Kundu DJ, Kamatchinathan S, Bai J, Hewapathirana S, et al. The PRIDE database at 20 years: 2025 update. Nucleic Acids Res. 2025;53(D1):D543–53.
89. Hammal F, de Langen P, Bergon A, Lopez F, Ballester B. ReMap 2022: a database of Human, Mouse, Drosophila and Arabidopsis regulatory regions from an integrative analysis of DNA-binding sequencing experiments. Nucleic Acids Res. 2022;50(D1):D316–25.
90. Robinson JT, Thorvaldsdottir H, Winckler W, Guttman M, Lander ES, Getz G, et al. Integrative genomics viewer. Nat Biotechnol. 2011;29(1):24–6.

Publisher's note